Bacterial coexistence driven by motility and spatial competition

https://doi.org/10.1038/s41586-020-2033-2

Received: 24 October 2018

Accepted: 17 December 2019

Published online: 19 February 2020

Check for updates

Sebastian Gude[1], Erçağ Pinçe[1,2], Katja M. Taute[1,2], Anne-Bart Seinen[1], Thomas S. Shimizu[1]✉ & Sander J. Tans[1,3]✉

Elucidating elementary mechanisms that underlie bacterial diversity is central to ecology[1,2] and microbiome research[3]. Bacteria are known to coexist by metabolic specialization[4], cooperation[5] and cyclic warfare[6–8]. Many species are also motile[9], which is studied in terms of mechanism[10,11], benefit[12,13], strategy[14,15], evolution[16,17] and ecology[18,19]. Indeed, bacteria often compete for nutrient patches that become available periodically or by random disturbances[2,20,21]. However, the role of bacterial motility in coexistence remains unexplored experimentally. Here we show that—for mixed bacterial populations that colonize nutrient patches—either population outcompetes the other when low in relative abundance. This inversion of the competitive hierarchy is caused by active segregation and spatial exclusion within the patch: a small fast-moving population can outcompete a large fast-growing population by impeding its migration into the patch, while a small fast-growing population can outcompete a large fast-moving population by expelling it from the initial contact area. The resulting spatial segregation is lost for weak growth–migration trade-offs and a lack of virgin space, but is robust to population ratio, density and chemotactic ability, and is observed in both laboratory and wild strains. These findings show that motility differences and their trade-offs with growth are sufficient to promote diversity, and suggest previously undescribed roles for motility in niche formation and collective expulsion–containment strategies beyond individual search and survival.

To study the role of spatial exploration in bacterial coexistence, we grew mixed populations in soft gels or liquid cultures. Bacteria can actively spread through low-density agar gels by their motility[9], whereas they are dispersed passively throughout liquid cultures by shaking. Two wild *Escherichia coli* strains A and B isolated from faecal samples of a single host[22] (a cohabitant pair) that could be transformed with plasmids carrying YFP and CFP markers, were mixed in different ratios R_0 and then inoculated in a shaken flask or as a spot in a soft-agar gel (35 mm in diameter, around 4 mm high) (Fig. 1a). After a growth period of 2.5–4 days at 33.5 °C, the fold change in the population ratio (R = A/B) was quantified by plating the strains on hard agar and counting the number of colony-forming units, after first dissolving the entire gel and its contents into fresh medium. In the shaken flasks, we found that R increased about 1,000-fold. This competitive advantage of A was independent of R_0 (Fig. 1b), as expected for strains that grow independently. By contrast, the gel experiments showed a notable dependence: R increased (fold change > 1) at low R_0, while R decreased (fold change < 1) at high R_0 (Fig. 1c). In other words, A was found to outcompete B when A was initially low in relative abundance, whereas B outcompeted A when B was initially low in relative abundance.

Selection that depends negatively on population frequency, as observed here (Fig. 1c), is considered key to coexistence[1,2]. When such negative selection functions fail to cross the R fold change = 1 line, one population is still outcompeted at all initial frequencies and thus driven to extinction (Fig. 1d). Stable coexistence is therefore defined strictly by an inversion in competitive hierarchy[23,24]: both populations must be able to outcompete the other when low in frequency. The populations are then driven to a fixed point at which both coexist (Fig. 1d). Such a hierarchy inversion is observed for A and B in the gel environment (Fig. 1c). Other wild cohabitant pairs and gels with a different medium also showed negative selection functions and hierarchy inversion (Extended Data Fig. 1).

To investigate the underlying causes of hierarchy inversion in static gels, we developed a method to quantify spatial population distributions, based on calibrated tile-scan fluorescence microscopy (Extended Data Fig. 2). When inoculated individually as monocultures, A and B spread through the entire gel within 4 days (Fig. 2a). By contrast, when inoculated as a mixed culture (R_0 = 1), A now remained confined to a small proximal area around the point of inoculation (diameter of approximately 5.6 mm), while B was observed only in the distal gel region outside the area occupied by A, at the gel periphery (Fig. 2a). The initially mixed A and B populations thus excluded each other spatially: the presence of A led to the displacement of the B population from the proximal region, while B impeded the spread of the A population to the distal region (Fig. 2a). Consistently, other strain pairs that exhibited negative selection functions (three out of five pairs) also showed such

[1]AMOLF, Amsterdam, The Netherlands. [2]Rowland Institute at Harvard University, Cambridge, MA, USA. [3]Bionanoscience Department, Kavli Institute of Nanoscience Delft, Delft University of Technology, Delft, The Netherlands. ✉e-mail: shimizu@amolf.nl; tans@amolf.nl

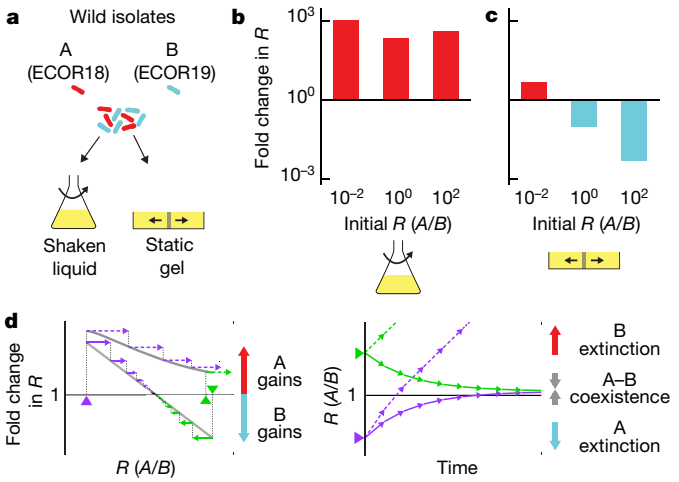

Fig. 1 | Inversion of competition hierarchy for cohabitant wild isolates. **a**, Two wild strains, A and B, were isolated from a single host[22], labelled with YFP and CFP, and inoculated at initial ratio R or $R_0 = A_0/B_0$ into a well-mixed (shaken flask) or non-mixed (soft-agar plate) environment. Final ratio ($R_1 = A_1/B_1$) was quantified by colony counting. **b**, **c**, Selection curves: ratio fold change (R_1/R_0) against R_0. In the well-mixed environment, A always outcompetes B (**b**). In the non-mixed habitat, A outcompetes B at low R_0, while B outcompetes A at high R_0, indicating a hierarchy inversion (**c**). **d**, Hierarchy inversion and stable coexistence. Left, selection curve without (top curve) or with hierarchy inversion (bottom curve crosses the $R = 1$ line). Right, corresponding temporal development of R, for repeated cycles of growth (arrows) followed by population bottlenecks. Starting population at low (purple) or high (green) initial ratio. No hierarchy inversion: A wins consistently, resulting in extinction of B (dashed arrows all point to the right in the left panel). With hierarchy inversion: A wins at low R_0 and low A_0 (solid arrows point to the right), while B wins at high R_0 and low B_0 (solid arrows point to the left), thus driving the populations to an equilibrium ratio that is independent of R_0 (right panel), a hallmark of stable coexistence.

reciprocal spatial exclusion (Extended Data Fig. 1). Inoculation around the gel edge rather than in the centre inverted the pattern: B now occupied the gel centre and A the periphery (Extended Data Fig. 3a). Thus, B was consistently excluded from a region proximal to the inoculation area, and A from a region distal to the inoculation area.

Bacterial populations have been shown to inhibit each other by secreting antibiotics[8], and can also interact using metabolites[25], chemotactic cues[9] and quorum sensing[26]. Theory suggests that cyclical inhibitory interactions between motile strains can segregate mixed populations in uniform environments[6,7]. Most strains were indeed motile and chemotactic (80% of isolates) (Extended Data Fig. 3b). However, tests for secreted compounds that inhibit cell growth were negative (Extended Data Fig. 4). The observed segregation also differs from sectoring in closely packed bacterial colonies on hard-agar gels[27] and in biofilms[25]. However, we noticed a pattern in measured growth and migration propensities for the segregating strain pairs: if one had a growth advantage, then the other typically had a migration advantage (Fig. 2b). One pair lacked such a growth–migration trade-off and indeed did not display reciprocal spatial exclusion (Fig. 2b and Extended Data Fig. 1). Another pair appeared inconsistent with this simple pattern, by showing a trade-off but no spatial exclusion, although the migration rates were nearly identical and hence the trade-off was weak (Fig. 2b and Extended Data Fig. 1).

To test whether growth–migration trade-offs have a role in segregation, we engineered *E. coli* laboratory strains with altered migration and growth propensities, by replacing the chemotaxis regulator *cheY* with an inducible constitutively active variant, and by introducing plasmids that conferred growth penalties. Spatial exclusion was absent or weak when migration and growth propensities were similar (Fig. 2c, g). We did observe distal (peripheral), but not proximal (central) exclusion when migration differed but growth was similar (Fig. 2d, g). Distal and proximal (reciprocal) exclusion was observed when growth and migration both differed and exhibited a trade-off (Fig. 2e, g). Thus, strains that were identical except for the migration and growth modifications excluded each other, indicating that specific interactions such as toxin secretion were not required.

Examination of the colonization dynamics revealed that unexpected collective strategies occurred under the growth–migration trade-offs. We measured the distributions of the wild strains A and B over time (Fig. 3a) and found them to be strikingly similar to predictions by a Keller–Segel[28] bacterial motility model (Fig. 3b). Notably, we extended the latter with Monod growth, nutrient consumption and diffusion, and used only independently measured growth rates and migration speeds from monocultures as input, with no additional fitted parameters. This Monod–Keller–Segel (MKS) model accurately predicted key qualitative features of the data, while quantitative aspects such as exact sizes of occupied territories differed (Extended Data Fig. 5e–l). This analysis shows how a shared nutrient pool can lead to indirect inhibitory interactions that drive spatial exclusion.

On the one hand, fast movers constrain slow movers within the proximal region. By consuming all local nutrients at the colony edge and those flowing inwards from the distal region, the former can block the nutrient influx to the proximal region. This cut-off of nutrient supply is completed at around 1.6 days, abruptly arresting growth of the slow movers (Fig. 3c) and impeding their migration (Fig. 3d), after which the fast movers capture the distal territory without competition (Fig. 3a, b). On the other hand, slow movers (yet fast growers) can win the proximal territory by dominating nutrient consumption there until the cut-off occurs and therefore limit the proximal population growth of faster movers (yet slow growers) (Fig. 3a–c). Furthermore, by rapidly depleting nutrients, they accelerate the formation of nutrient gradients that stimulate the departure of their fast-moving competitors from the proximal region (Extended Data Fig. 6a).

Several other aspects of this mechanism are notable. First, it involves two (co)migrating population fronts. A priori, both can reach the gel edge albeit at different times. The lagging population can then dominate everywhere by growing faster. Here we find that fast-moving fronts readily arrest migration of slower-moving ones and thus promote coexistence. Second, how territory and competition relate is not immediately intuitive: the strains competed better when rare (Fig. 3f), but then seized smaller territories (Fig. 3e). These opposing trends are not incompatible, however, as populations can achieve greater relative growth when they are initially smaller and limited by carrying capacity, even when their territory shrinks. Third, the segregation itself is very robust. Note that the initial frequency of fast movers can be low and will first decrease even further because of slow growth. However, despite being outnumbered by several orders of magnitude, they can still contain their fast-growing competitors by forming a thin encapsulating shell (Fig. 3e, f). Overall, effective niches are thus formed in which both populations can re-establish when rare and can therefore coexist. In contrast to classic pre-existing spatial niches[24], however, here the niches emerge from reciprocal interactions between strains within an initially uniform environment.

If these reciprocal interactions indeed stabilize mixed populations, then shifting their balance should drive subpopulations to altered equilibria or even extinction (Fig. 4a, b). The fast movers (yet slow growers) should become increasingly deprived of their distal niche in smaller gels or more generally when virgin space is lacking. Conversely, the advantage of fast growers (yet slow movers) should diminish when their proximal niche provides less growth headroom. Indeed, the MKS model indicated how coexistence can break down with large changes in patch size (Fig. 4c), inoculation density (Fig. 4d) and trade-off strength (Fig. 4e). Experimental tests indeed showed that fast movers lost their ability to invade fast growers when inoculated across the entire gel surface rather than in a spot, as there was no virgin space (Fig. 4f).

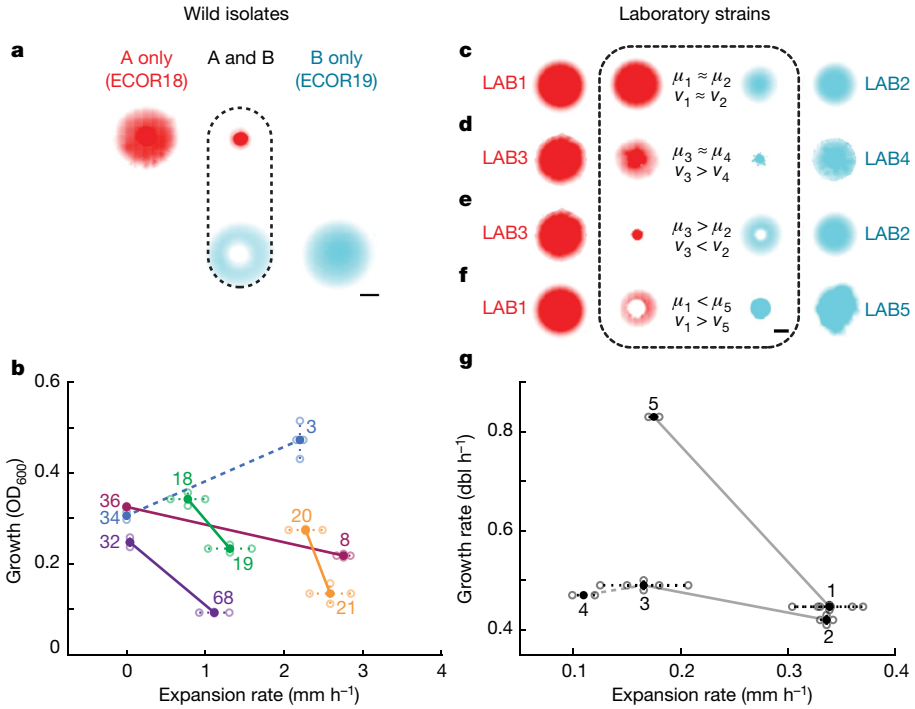

Fig. 2 | Growth–migration trade-offs and spatial exclusion. a, Tile-scanned fluorescence micrographs quantifying the spatial distributions of wild isolates A and B in soft-agar gels. Monocultures spread through the entire gel (35 mm diameter). As co-cultures ($R_0 = 1$), A and B spontaneously segregate: A is excluded distally (from the inoculum), B is excluded proximally. Scale bar, 7.5 mm. Gels contain glycerol minimal medium. **b**, Growth and migration in wild strain pairs, indicating a trade-off. Growth is quantified in shaken medium by optical density at 600 nm (OD_{600}) at 7.5 h. Migration rate is quantified as speed of the migrating front. Numbers, ECOR strain identifiers. Solid lines, cohabitant pairs showing a growth–migration trade-off. Dashed lines, pairs not showing a trade-off. In **b** and **g**, solid circles are global means, open circles are defined in the Methods, 'Statistics and reproducibility'. Medium: rich tryptone broth. **c**–**f**, Competition between strains with engineered growth (μ) and migration (v) rates. Monocultures (left and right) and mixed cultures ($R_0 = 1$; middle) indicated: no exclusion for weak or no differences in μ and v (**c**), one-way exclusion for small difference in v only (**d**), two-way (reciprocal) exclusion for significant trade-off between μ and v (**e**, **f**). Scale bar, 7.5 mm. Medium: minimal glycerol. **g**, Growth (in doublings (dbl) h^{-1}) and migration quantification for engineered strains (**c**–**f**). Numbers are strain identifiers, lines indicate competing strains. Medium: minimal glycerol.

Conversely, the fast growers showed a decrease in overall competitive advantage when the growth headroom was reduced by inoculating the strains at high total density (Fig. 4g) or when the trade-off weakens by limiting the growth advantage of the fast-growing strain (Fig. 4h).

Coexistence was also robust to the mode of motility (Extended Data Fig. 6), changes in patch and inoculation geometry (Extended Data Figs. 5c, d, 7a–j), separate inoculation locations for both strains[19] (Extended Data Fig. 7k–m) and the presence of additional strains (Extended Data Fig. 5a, b). For instance, coexistence was similarly observed for mixed cultures that were inoculated on the outside of a spherical nutrient patch and thus migrated inwards (Extended Data Fig. 7j). Also note that the motile but non-chemotactic, *cheY*-modified strains migrated collectively as a Fisher wave[29] and arrested the migration of slower-moving strains (Fig. 2d). The 'pushed' nature[30] of chemotactic waves is thus not essential for segregation and coexistence. However, chemotaxis does offer competitive advantages through improved spatial exclusion and invasibility (Extended Data Fig. 6e–j). Exclusion was also not limited to within-species pairs as indicated by a segregating *E. coli*–*Salmonella* pair (LAB1–LAB5 in Fig. 2f, g).

Finally, we wondered about the origins of the observed growth–migration trade-off. Genome sequence analysis suggested a potentially complex genetic basis, as more than 50 amino acid substitutions were detected between strains A and B across multiple motility genes (Extended Data Table 1). Three-dimensional single-cell tracking of all wild isolates revealed large differences in swimming speed among strains, which correlated well with their population migration speeds (Fig. 2b and Extended Data Fig. 8). These data suggested a functional basis for the trade-off: in contrast to other migration factors such as chemotactic navigation, swimming requires the expression and operation of a large propulsion machinery of flagella, and can therefore limit growth through metabolic costs. To further test this idea, we engineered strains to independently vary the expression of flagella. We found that swimming speeds increased while growth rates decreased as the expression of flagella was induced (Extended Data Fig. 9), which is indeed consistent with a cost-based motility–growth trade-off. Other evidence of general growth–migration trade-offs among bacteria has previously been reported[16,17,31].

Motility has been a defining feature of bacteria since they were first observed by van Leuwenhoek[32], and has been studied extensively in mechanistic terms[9]. Here we report that motility can have a direct role in promoting bacterial diversity. Key is the cyclic competitive colonization of nutrient patches, which produces effective niches for strains with different migration speeds and their associated growth trade-offs, without requiring specific signalling or inhibition between cells. The mechanism is not only reminiscent of competition–colonization models that have been developed for plant ecosystems[24,33], in which poor local competitors prevent extinction by better seed dispersal, but also contains elements of overgrowth competition models applied to biofilms[2] and plants[32], in which one species physically covers another to compete for light or other resource fluxes. Our findings raise new questions regarding the role of community diversity in shaping selective pressures on motility, and may contribute to explaining the broad range of bacterial motility phenotypes observed in nature. More generally, cycles of spatial competition for virgin territories are prevalent in diverse ecosystems that undergo disturbances, such as host feeding cycles, windfall, pathogen transmission, forest fires and changes in climate, and have long been speculated to influence natural communities[34]. Therefore, motility-based mechanisms for coexistence akin

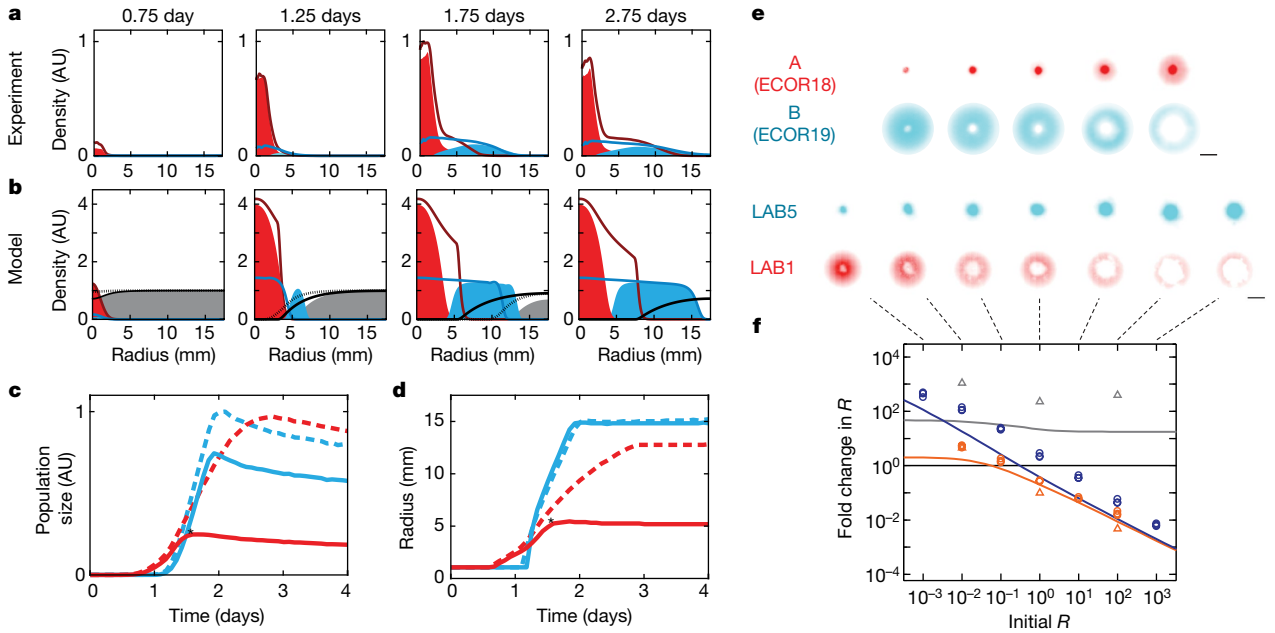

Fig. 3 | Expulsion and containment in competitive migration. a, Spatial density profiles along colony radius for wild strains A (red) and B (blue) competing in a gel, for the indicated times after inoculation. Solid curves: monocultures. Shaded regions: co-cultures ($R_0 = 1$). **b**, Spatial density profiles from MKS model simulations. Definitions as in **a**. Nutrient density profiles for A only (black solid curve), B only (dotted curve), co-culture (grey shaded region). **c**, Measured population size versus time for A (red) and B (blue). Dashed curves: monocultures. Solid curves: co-cultures ($R_0 = 1$). **d**, Measured migration-front radius versus time. Definitions are as in **c**. **e**, Tile-scan fluorescence micrographs for co-cultures for different initial (inoculation) ratios R_0 (see **f**). Scale bars, 10 mm. **f**, Selection curves from measurements (points) and MKS model (solid lines). Red, A–B in gel; dark blue, LAB5–LAB1 in gel; grey, A–B in shaken culture. Circles, quantification of fluorescence microscopy images. Triangles, colony-counting quantification (data as in Fig. 1). Using parameters from monocultures, the MKS model correctly predicts hierarchy inversion. Medium: minimal glycerol (all panels). AU, arbitrary units.

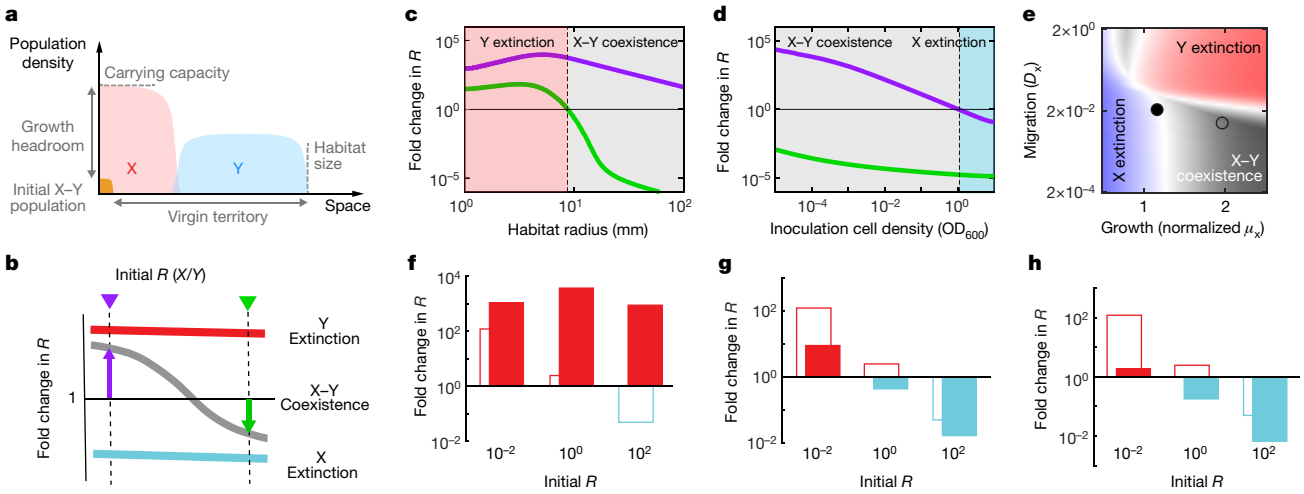

Fig. 4 | Stability of coexistence and its limits. a, Factors limiting stability. The advantage of a fast mover (Y) is limited by a smaller virgin territory, and hence habitat size. The advantage of a fast grower (X) is limited by growth headroom (carrying capacity over initial population density, see **c**, **d**). **b**, The stability of coexistence is assessed by the lengths of purple and green arrows (Methods). **c**, Effect of habitat size. Computed fold change in X/Y (that is, LAB5/LAB1) as a function of habitat radius, for low and high initial ratios (purple and green, see **b**). Grey region, coexistence, as purple is above unity and green below. Red region, X outcompetes Y for small habitats. **d**, Effect of total initial cell density. Blue region, Y outcompetes X, with X extinction only for cell densities close to carrying capacity. **e**, Effect of growth–migration trade-off. Computed coexistence phase diagram for X and Y. Axis indicate X growth rate normalized by Y growth rate, and motility of X, with Y parameters fixed and equal to LAB1. Coexistence (grey), Y extinction (red) and X extinction (blue), and intensity indicating stability (**b**). White, transition region. Open circle, LAB5–LAB1 having a strong trade-off. Closed circle, approximate position of LAB3–LAB2 having weaker trade-off. **f**, Competition data suppressed virgin territory (LAB5–LAB1). Open bars, reference spot-inoculated data. Solid bars, strain mixtures were spread over the entire gel surface. Consistent with predictions (**c**), the fast grower (LAB5) outcompetes the fast mover (LAB1). **g**, Competition data at high inoculation density. Open bars, reference; see **f**. Solid bars, pelleted LAB5–LAB1 mixtures were inoculated. Consistent with predictions (panel d), fast mover (LAB1) now competes better. **h**, Competition data for smaller trade-off. Open bars: reference, see **f**. Solid bars, LAB3–LAB2 competition data. The fast mover (LAB2) now competes better overall, consistent with a smaller growth advantage, and proximity to the blue region (**e**). Medium: minimal glycerol.

to the one studied here may be broadly relevant for understanding species diversity throughout nature.

Online content

Any methods, additional references, Nature Research reporting summaries, source data, extended data, supplementary information, acknowledgements, peer review information; details of author contributions and competing interests; and statements of data and code availability are available at https://doi.org/10.1038/s41586-020-2033-2.

1. Rainey, P. B., Buckling, A., Kassen, R. & Travisano, M. The emergence and maintenance of diversity: insights from experimental bacterial populations. *Trends Ecol. Evol.* **15**, 243–247 (2000).
2. Hibbing, M. E., Fuqua, C., Parsek, M. R. & Peterson, S. B. Bacterial competition: surviving and thriving in the microbial jungle. *Nat. Rev. Microbiol.* **8**, 15–25 (2010).
3. Koskella, B., Hall, L. J. & Metcalf, C. J. E. The microbiome beyond the horizon of ecological and evolutionary theory. *Nat. Ecol. Evol.* **1**, 1606–1615 (2017).
4. Turner, P. E., Souza, V. & Lenski, R. E. Tests of ecological mechanisms promoting the stable coexistence of two bacterial genotypes. *Ecology* **77**, 2119–2129 (1996).
5. Ross-Gillespie, A., Gardner, A., West, S. A. & Griffin, A. S. Frequency dependence and cooperation: theory and a test with bacteria. *Am. Nat.* **170**, 331–342 (2007).
6. Kerr, B., Riley, M. A., Feldman, M. W. & Bohannan, B. J. Local dispersal promotes biodiversity in a real-life game of rock–paper–scissors. *Nature* **418**, 171–174 (2002).
7. Reichenbach, T., Mobilia, M. & Frey, E. Mobility promotes and jeopardizes biodiversity in rock–paper–scissors games. *Nature* **448**, 1046–1049 (2007).
8. Kelsic, E. D., Zhao, J., Vetsigian, K. & Kishony, R. Counteraction of antibiotic production and degradation stabilizes microbial communities. *Nature* **521**, 516–519 (2015).
9. Berg, H. C. Motile behavior of bacteria. *Phys. Today* **53**, 24–29 (2000).
10. Parkinson, J. S., Hazelbauer, G. L. & Falke, J. J. Signaling and sensory adaptation in *Escherichia coli* chemoreceptors: 2015 update. *Trends Microbiol.* **23**, 257–266 (2015).
11. Alon, U., Surette, M. G., Barkai, N. & Leibler, S. Robustness in bacterial chemotaxis. *Nature* **397**, 168–171 (1999).
12. Ames, P. & Bergman, K. Competitive advantage provided by bacterial motility in the formation of nodules by *Rhizobium meliloti*. *J. Bacteriol.* **148**, 728–729 (1981).
13. Stocker, R., Seymour, J. R., Samadani, A., Hunt, D. E. & Polz, M. F. Rapid chemotactic response enables marine bacteria to exploit ephemeral microscale nutrient patches. *Proc. Natl Acad. Sci. USA* **105**, 4209–4214 (2008).
14. Roszak, D. B. & Colwell, R. R. Survival strategies of bacteria in the natural environment. *Microbiol. Rev.* **51**, 365–379 (1987).
15. Vergassola, M., Villermaux, E. & Shraiman, B. I. 'Infotaxis' as a strategy for searching without gradients. *Nature* **445**, 406–409 (2007).
16. Fraebel, D. T. et al. Environment determines evolutionary trajectory in a constrained phenotypic space. *eLife* **6**, e24669 (2017).
17. Yi, X. & Dean, A. M. Phenotypic plasticity as an adaptation to a functional trade-off. *eLife* **5**, e19307 (2016).
18. Grossart, H.-P., Riemann, L. & Azam, F. Bacterial motility in the sea and its ecological implications. *Aquat. Microb. Ecol.* **25**, 247–258 (2001).
19. Song, H., Payne, S., Gray, M. & You, L. Spatiotemporal modulation of biodiversity in a synthetic chemical-mediated ecosystem. *Nat. Chem. Biol.* **5**, 929–935 (2009).
20. Lehman, J. T. & Scavia, D. Microscale patchiness of nutrients in plankton communities. *Science* **216**, 729–730 (1982).
21. Blackburn, N., Fenchel, T. & Mitchell, J. Microscale nutrient patches in planktonic habitats shown by chemotactic bacteria. *Science* **282**, 2254–2256 (1998).
22. Ochman, H. & Selander, R. K. Standard reference strains of *Escherichia coli* from natural populations. *J. Bacteriol.* **157**, 690–693 (1984).
23. Chesson, P. Mechanisms of maintenance of species diversity. *Annu. Rev. Ecol. Syst.* **31**, 343–366 (2000).
24. Jeltsch, F. et al. Integrating movement ecology with biodiversity research - exploring new avenues to address spatiotemporal biodiversity dynamics. *Mov. Ecol.* **1**, 6 (2013).
25. Liu, J. T. et al. Metabolic co-dependence gives rise to collective oscillations within biofilms. *Nature* **523**, 550–554 (2015).
26. Miller, M. B. & Bassler, B. L. Quorum sensing in bacteria. *Annu. Rev. Microbiol.* **55**, 165–199 (2001).
27. Hallatschek, O., Hersen, P., Ramanathan, S. & Nelson, D. R. Genetic drift at expanding frontiers promotes gene segregation. *Proc. Natl Acad. Sci. USA* **104**, 19926–19930 (2007).
28. Keller, E. F. & Segel, L. A. Traveling bands of chemotactic bacteria: a theoretical analysis. *J. Theor. Biol.* **30**, 235–248 (1971).
29. Houchmandzadeh, B. & Vallade, M. Fisher waves: an individual-based stochastic model. *Phys. Rev. E* **96**, 012414 (2017).
30. Gandhi, S. R., Yurtsev, E. A., Korolev, K. S. & Gore, J. Range expansions transition from pulled to pushed waves as growth becomes more cooperative in an experimental microbial population. *Proc. Natl Acad. Sci. USA* **113**, 6922–6927 (2016).
31. Ni, B. et al. Evolutionary remodeling of bacterial motility checkpoint control. *Cell Rep.* **18**, 866–877 (2017).
32. Dobell, C. *Antony Van Leeuwenhoek and His Little Animals* (John Bale, Sons & Danielsson, 1960).
33. Levin, S. A. Dispersion and population interactions. *Am. Nat.* **108**, 207–228 (1974).
34. Sousa, W. P. The role of disturbance in natural communities. *Annu. Rev. Ecol. Syst.* **15**, 353–391 (1984).

Methods

Data reporting

No statistical methods were used to predetermine sample size. The experiments were not randomized and the investigators were not blinded to allocation during experiments and outcome assessment.

Culture medium and growth conditions

For growth–migration experiments in minimal medium H1 (MMH1) (50 mM KPO_4, 7.6 mM $(NH_4)_2SO_4$, 0.5 mM $MgSO_4$, 1.25 μM $Fe_2(SO_4)_3$, 67 mM NaCl, 0.01% w/v thiamine, pH 7.0) soft-agar plates, pre-cultures of bacteria were directly inoculated from glycerol stocks and grown in 2 ml tryptone broth (TB, 1% w/v tryptone and 0.5% w/v NaCl) at 30 °C, 250 rpm, supplemented with antibiotics (100 μg ml^{-1} ampicillin and 34 μg ml^{-1} chloramphenicol) for approximately 8 h. Overnight cultures were started by diluting pre-cultures 1:100 into 10 ml fresh MMH1 supplemented with 0.1% v/v glycerol, amino acids (1 mM L-histidine, 1 mM L-methionine, 1 mM L-leucine, 1 mM L-threonine and 100 μM L-asparagine) and antibiotics, and grown overnight at 33.5 °C, 250 rpm. Day cultures were started by diluting overnight cultures to an OD_{600} of 5×10^{-3} in 10 ml MMH1 supplemented with glycerol, amino acids, antibiotics and inducers (100 μM isopropyl-β-D-1-thiogalactopyranoside (IPTG) and 0.75 μM sodium salicylate) and grown at 33.5 °C, 250 rpm until early-exponential phase (OD_{600} of approximately 0.1). Bacterial densities were adjusted to $OD_{600} = 0.01$ from day cultures. For competition experiments, strains were mixed 1:1 or as indicated. Competition medium consisted of MMH1 supplemented with glycerol, amino acids, antibiotics and inducers. Soft-agar plates were prepared in small Petri dishes (Falcon Easy Grip Petri Dish, polystyrene, 35 × 10 mm style) by supplementing 4 ml competition medium with 0.26% (w/v) bacto agar (DB). Then, 2 μl of OD_{600}-adjusted bacterial culture was inoculated in the centre of the soft-agar plate (if not otherwise specified). Soft-agar plates were incubated for 4 days at 33.5 °C. A humid environment was mediated by placing a water reservoir close by within the incubation chamber. For growth–migration experiments in TB soft-agar plates, pre-cultures of bacteria were directly inoculated from glycerol stocks and grown overnight in 2 ml TB supplemented with antibiotics at 30 °C, 250 rpm. First-day cultures were started by diluting pre-cultures 1:100 into 10 ml fresh TB supplemented with antibiotics and inducers, and grown at 33.5 °C, 250 rpm, until mid-exponential phase (OD_{600} of 0.4–0.8). Subsequently, second-day cultures were started by diluting first-day cultures to an OD_{600} of 5×10^{-3} in 10 ml fresh liquid TB medium supplemented with antibiotics and inducers and grown at 33.5 °C, 250 rpm, until early exponential phase (OD_{600} 0.2–0.3). Bacterial densities were adjusted to $OD_{600} = 0.01$ from day cultures. For competitions, strains were mixed 1:1 or as indicated. TB supplemented with antibiotics and inducers was prepared. TB-based soft-agar plate preparation, inoculation and incubation were prepared as described above for MMH1 soft-agar plates.

For competition in well-mixed (shaken liquid culture) conditions, the protocol up until the mixing of strains was identical to that for the competition experiments on soft-agar plates, but inoculation was into 10 ml competition medium, with subsequent growth at 33.5 °C, 250 rpm, for 60 h, during which time saturation was reached. The initial OD_{600} was adjusted to match the initial ratio of bacteria to nutrients in soft-agar plates.

Bacterial growth measurements

For the growth-rate measurement of ECOR18, ECOR19 and LAB strains, pre-cultures of bacteria were directly inoculated from glycerol stocks and grown in 2 ml TB at 30 °C, 250 rpm, supplemented with antibiotics for approximately 8 h. Overnight cultures were started by diluting pre-cultures 1:100 into 10 ml fresh MMH1 supplemented with glycerol, amino acids and antibiotics and grown overnight at 33.5 °C, 250 rpm. Day cultures were started by diluting overnight cultures to an OD_{600} of 5×10^{-3} in 10 ml MMH1 supplemented with glycerol, amino acids, antibiotics and inducers and grown at 33.5 °C, 250 rpm until early-exponential phase (OD_{600} of approximately 0.1). The OD_{600} of cells grown inside the final sub-culture was adjusted to 5×10^{-3} in 5 ml fresh MMH1 supplemented with glycerol, amino acids, antibiotics and inducers, and distributed into the wells of Costar assay plates (96-well flat-bottom polystyrene plates) in a volume of 200 μl. The growth was measured using a Perkin Elmer Victor X3 plate reader at 33.5 °C. Growth rates were extracted from early-mid exponential phase in competition medium. Mean growth rates were calculated by averaging over several replicates (see 'Statistics and reproducibility' for details), that is, wells within one 96-well plate.

For the growth-yield measurement of ECOR strains, each strain was inoculated into Luria–Bertani (LB, 1% (w/v) tryptone, 0.5% (w/v) yeast extract, 0.5% (w/v) NaCl) hard agar (1.5% (w/v)) as stab cultures from glycerol stocks and incubated at 37 °C for approximately 4.5 h. Stab-culture-grown cells were picked using a sterile tip and inoculated into 1 ml of fresh TB and grown overnight at 33.5 °C at 250 rpm. Overnight cultures of each strain were diluted 1:1,000 into 1 ml fresh TB and distributed over 96-well plate. The OD_{600} of each wild isolate strain (ECOR3, ECOR8, ECOR18, ECOR19, ECOR20, ECOR21, ECOR32, ECOR34, ECOR36 and ECOR68) was measured to assess the growth yield at 7.5 h in 96-well plates shaken at 282 rpm at 34 °C (see 'Statistics and reproducibility' for details).

For three-dimensional tracking, staining of the flagella and growth rate measurements of flagellar induction and control strains (TSS1410 and TSS1709, respectively), overnight cultures were directly inoculated from glycerol stocks and grown to saturation at 30 °C, 250 rpm, in 2 ml TB, supplemented with antibiotics and 5 mM galactose. Overnight cultures (20 μl) were inoculated into 10 ml MMH1 supplemented with 5 mM galactose, amino acids (1 mM L-histidine, 1 mM L-methionine, 1 mM L-leucine and 1 mM L-threonine) and antibiotics, and grown at 33.5 °C, 250 rpm. For growth-rate measurements, exponential-phase cultures were diluted to an OD_{600} of 10^{-3} into MMH1 supplemented with 5 mM galactose, amino acids, antibiotics and inducers (0.5 μM sodium salicylate, variable IPTG as indicated), and growth rates were obtained from plate-reader experiments as for the LAB strains (see 'Statistics and reproducibility' for details).

Swimming-speed measurements

Three-dimensional tracking using phase-contrast microscopy[35] was performed on freshly collected bacteria diluted to an OD_{600} of 0.005–0.01 and placed in chambers consisting of a slide and #1 cover glass separated by two strips of three layers of parafilm and sealed with molten valap (vaseline, lanolin and paraffin). Recordings were obtained at 15 Hz on a Nikon inverted optical microscope equipped with an air condenser (Nikon LWD, numerical aperture (NA) 0.52) and a 40× phase-contrast lens (Nikon, S Plan Fluor ELWD, 40×, Ph2, NA 0.6, correction collar set to 1.2 mm) as well as a PCO.edge sCMOS camera.

For flagellar induction and control strains (TSS1410 and TSS1709), bacteria were diluted into motility medium (10 mM KPO_4, 0.1 mM EDTA, 1 μM L-methionine, 10 mM lactic acid and 67 mM NaCl, pH 7.0) supplemented with 0.18% (hydroxypropyl)methyl cellulose. For each condition reported, a total of 2–6 acquisitions of 1,500 frames each were recorded on 1 or 2 different days. Trajectories with a duration longer than 5 frames, comprising a total of 2.9×10^5 s of trajectory time, were retained for analysis. Instantaneous swimming speeds were computed as the fourth-order central difference[36]. Bacteria with a median speed lower than 17 μm s^{-1} were deemed immotile. The mean instantaneous speed across all trajectories and all time points and the standard error of the mean were computed for each acquisition, and the overall mean for each condition was computed as the average between acquisitions, weighted by the standard error of the mean.

For ECOR strains, each bacterial strain was directly inoculated from glycerol stocks onto LB hard-agar plates supplemented with antibiotics

and grown overnight at 34 °C. Grown single colonies were picked using sterile tips, separately inoculated in 2.5 ml fresh TB supplemented with antibiotics and grown overnight at 33.5 °C, 220 rpm. The day cultures were started by diluting overnight cultures 1:1,000 in 10 ml fresh TB supplemented with antibiotics and the inducer (100 μM IPTG) and grown at 33.5 °C, 220 rpm until reaching an OD_{600} of 0.3–0.4. Cells were diluted into fresh TB for tracking. For each strain, a total of 3–7 acquisitions of 1,500 frames were recorded on 1 or 2 different days. Trajectories were smoothed using second-order trend filtering based on ADMM (Alternating Direction Method of Multipliers)[37]. The mean swimming speed of each strain was calculated by ensemble-averaging the instantaneous speed values of the total cell population obtained across all acquisitions.

Staining of the flagella

Collected cells were washed in motility medium three times, with centrifugation washes at 4,500*g* for 5 min. Subsequently, 10 μl of bacterial solution was placed between a slide and a coverslip coated with poly-L-lysine. Leifson stain solution[38] was prepared freshly by mixing 100 μl each of 1.2% basic fuchsin in ethanol, 1.5% sodium chloride in water and 3% tannic acid in water and vortexing the solution thoroughly. Then, 20 μl of stain was placed on the slide adjacent to the coverslip to slowly penetrate the sample. Samples were inspected by bright-field microscopy using a 100× oil-immersion lens.

Bacterial migration measurements using dark-field imager

For flagella induction strains, soft-agar plates, which consisted of 90-mm Petri dishes containing 25 ml MMH1, supplemented with 5 mM galactose, amino acids, antibiotics, inducers (0.5 μM sodium salicylate, variable IPTG as indicated), 100 μM aspartate and 0.26% (w/v) agar, were inoculated with 5 μl of saturated culture grown at 30 °C in 2 ml TB, supplemented with antibiotics and 5 mM galactose. Automated time-lapse images of plates were recorded using a custom-built dark-field imager with a rotary plate holding 6 Petri dishes, placed inside an incubator held at 33.5 °C. Colony expansion rates were extracted from a linear fit to the time series of colony radii obtained using a custom MATLAB ring-detection algorithm based on Hough transforms.

To measure expansion rate of wild isolates in TB medium, soft-agar plates consisting of 90-mm Petri dishes containing 50 ml TB, supplemented with 0.26% (w/v) agar, were inoculated with 20 μl day cultures. Before inoculation, wild isolate bacteria were directly inoculated from glycerol stocks and grown in 2 ml TB at 30 °C, 250 rpm until saturation. Day cultures were started by diluting pre-cultures 1:100 into 10 ml fresh TB and cultures were grown at 33.5 °C, 250 rpm until an OD_{600} between 0.4 and 0.6 was reached. Images of plates were acquired with a custom-built dark-field imager as described above for flagella induction strains. Colony expansion rates were extracted from a linear fit to the time series of colony radii obtained by manually tracking the colony front in ImageJ[39].

To observe migration phenotypes of wild isolates in LB medium, soft-agar plates, which consisted of 90-mm Petri dishes containing 25 ml LB supplemented with 0.26% (w/v) agar, were inoculated with 5 μl saturated cultures grown at 37 °C in 2 mL LB. Images of plates were acquired with a custom-built dark-field imager as described above for flagella induction strains.

Tile-scan microscopy

To record the growth-migration dynamics and spatial patterns of fluorescently labelled bacterial populations in small Petri dishes (35 × 10 mm style) a Nikon Eclipse TI inverted microscope was used with a Nikon 4×/ NA 0.13 Plan Fluor objective, a Hamamatsu Orca Flash 4.0 CMOS camera (2,024 × 2,024 pixels, pixel size 6.5 μm × 6.5 μm), a Lumencor Sola light engine LED and a motorized Märzhäuser scanning stage equipped with a custom Petri dish holder. The microscope body and the stage were encased by a custom-built incubation chamber equipped with temperature control. The microscope was controlled by custom-written scripts through μManager[40]. Plates were tile-scanned across a grid of image fields (11 × 11 images per plate; see Extended Data Fig. 2), with image acquisition at a focus approximately 1.5 mm above the bottom of the plate. Exposure times were automatically adjusted for each grid position to stay within the dynamic range of the camera. Images were binned 4 × 4 pixels using μManager software[40].

Image and data analysis of tile-scan microscopy data

Tile-scanned images of soft-agar plates were corrected for camera offset and illumination non-uniformity using fluorescence images of soft-agar gels wherein bacterial cells were homogeneously distributed, for each fluorescence channel individually. Subsequently, intensity values of each pixel were rescaled by the exposure time. Tile images were iteratively assembled into montages (Extended Data Fig. 2c) and resized by a factor 1/10 by downsampling using the built-in ImageJ[39] resize function without interpolation. Fluorescence intensities (I) were converted into proxies for bacterial densities (i).

$$I_{\mathrm{CFP}} = A_{\mathrm{CFPstrain}} D_{\mathrm{CFPstrain}} + B_{\mathrm{CFP}} + C_{\mathrm{CFP-YFP}} A_{\mathrm{YFPstrain}} D_{\mathrm{YFPstrain}} \quad (1)$$

$$I_{\mathrm{YFP}} = A_{\mathrm{YFPstrain}} D_{\mathrm{YFPstrain}} + B_{\mathrm{YFP}} + C_{\mathrm{YFP-CFP}} A_{\mathrm{CFPstrain}} D_{\mathrm{CFPstrain}} \quad (2)$$

Slopes A and background intensities B were obtained by linear fitting of equations (1) and (2) to mean fluorescence intensities extracted from calibration plates, that is, soft-agar plates of homogeneously spread monocultures of YFP- and CFP-labelled strains of known population size (Extended Data Fig. 2a, b). These calibration plates were prepared from liquid monocultures of cells expressing YFP or CFP at pre-adjusted OD_{600} values and supplementing each monoculture with 0.26% (w/v) agar. Once the soft-agar mixtures inside Petri dishes set at room temperature, the calibration plates were imaged in an 11 × 11 grid of tiles for each fluorescence channel at 4× magnification and the mean fluorescence intensity was obtained for each calibration plate by averaging pixel values of a subset of the tile images (6 × 6) nearest to centre of the Petri dish. Crosstalk coefficients C were estimated by calculating the correlations of fluorescence intensities between two images of a single calibration plate acquired in YFP and CFP channels. Population sizes and radial density profiles were extracted from inside the Petri dishes. Petri dish location and colony centre were selected manually using ImageJ[39]. Population sizes were arbitrarily normalized to the maximum value of ECOR19 grown as a monoculture. Radial bacterial densities were normalized to the maximum bacterial radial density reached by a reference strain (arbitrarily chosen to be ECOR18) measured in soft-agar gels grown as a monoculture. Final population ratios were computed as the ratio of population sizes of the competing populations at the last time point of each experiment (around 4 days). Colony expansion was recorded by tracking (after departure from the region of inoculation) the population fronts in radial density profiles over time. Migration rate, v, of LAB strains was extracted by fitting a first-order polynomial to the linear part of the colony expansion time series. The original plate images showing the fluorescence map of strain B (Fig. 3e, top) was radially cropped by applying a circular clipping mask with an offset of 3.25 mm from the rim to remove the imaging artefact observed at the edge of plates.

Fluorescence-based colony counting

At the end of competition experiments in liquid, cultures were diluted to appropriate densities and spread onto hard-agar plates (competition medium supplemented with 1.5% (w/v) agar). Similarly, the gel from soft-agar plate competitions were first dissolved by applying heat (8 min at 40 °C) followed by manual shaking and after which the gel was diluted and spread out. Hard-agar plates were incubated for 24–48 h at 37 °C and subsequently imaged by tile scanning using a Nikon 2×/NA 0.10 Plan Apo objective. Focus was adjusted manually in bright field onto

the colonies. Fluorescence was imaged in YFP and CFP channels while the exposure time was kept fixed for each fluorescence channel. Images were not corrected in any way. Colonies were counted manually using ImageJ[39]. Population ratios were obtained as ratios of colony counts in the respective fluorescence channels corrected by colony-forming efficiency of dissolved monoculture gels.

Genomics analysis

Sequencing reads of ECOR18 (SRR3951479) and ECOR 19 (SRR3951480) were obtained using the SRA Toolkit[41] v.2.9.2 fasterq-dump.2 with the parameter '--split-files'. Reads were trimmed by sickle[42] v.1.33 with the parameters 'pe -t sanger -q 20 -l 50' and aligned to the well-annotated reference sequence of *E. coli* strain MG1655 (U00096.3) with Bowtie2[43] v.2.3.4.3 using the parameters '-q --no-mixed --dovetail --very-sensitive --n-ceil L,0,0.001'. The resulting SAM files were sorted and converted to BAM format by Picard (http://broadinstitute.github.io/picard) v.2.18.25 SortSam and duplicates were marked using Picard MarkDuplicates. Variants were called individually for each strain using GATK[44] v.4.1.0.0 HaplotypeCaller with parameters '-ERC GVCF -ploidy 1'. The resulting .GVCF files were combined using gatk CombineGVCFs and genotyped by gatk GenotypeGVCFs with the parameter '-ploidy 1'. Variant calls were quality filtered twice using snpsift[45] v.4.3t filter using the parameters '--addFilter 'HFGlobal' '(DP<10) | (QD<2) | (FS>=60)'' and '--addFilter 'HFGenotype' '(GEN[*].GT=='.') | (GEN[*].DP<5) | (GEN[*].GQ<30)'' and marked calls were removed by VCFtools[46] v.0.1.15 using the parameters '--remove-filtered-all --recode --recode-INFO-all'. Variant calls were annotated by SnpEff[47] v.4.3t with parameters 'ann -v -no-upstream -no-downstream -no-intron' using a custom-build database of *E. coli* strain MG1655 (U00096.3). Only the assignment to genes was retained, while any additional annotations created by SnpEff were discarded as they characterize variants relative to the MG1655 reference. DNA and amino acid changes between ECOR18 and ECOR19 were subsequently annotated using a custom-written script for Python[48] v.3.6.7. In brief, the annotated VCF file created by SnpEff was imported and variant calls that were identical to both strains were discarded. Variant calls were split into those that occurred within genes and those that were annotated as 'intergenic'. Variants within genes were grouped by gene. For each gene, sequences of ECOR18 and ECOR19 were reconstructed by separately inserting variant calls into the MG1655 reference sequence. Genes containing small insertions or deletions or frameshifts were marked as such and not further annotated. All other genes were aligned relative to their start sites and DNA substitutions were annotated by pairwise comparison of individual DNA bases. Thereafter, gene sequences were translated using BioPython[49] v.1.72 and amino acid sequences were annotated by pairwise comparison as described above for the DNA sequences.

MKS model

The time evolution of spatial density profiles of motile populations, p_1 and p_2, was computed by numerically integrating a set of Keller–Segel equations[28] modified with a Monod growth term[50] coupled to a diffusing nutrient, n. We express the equations in polar coordinates and impose radial symmetry to reflect the conditions of the soft-agar experiment in Petri dishes. The model consists of three partial differential equations:

$$\frac{\partial p_1}{\partial t} = r^{-1}\frac{\partial}{\partial r}\left(r\frac{n}{K+n}\left(D_1\frac{\partial p_1}{\partial r} - \chi_1 p_1\frac{\partial n}{\partial r}\right)\right) + \ln 2\frac{n}{K+n}\mu_1 p_1$$

$$\frac{\partial p_2}{\partial t} = r^{-1}\frac{\partial}{\partial r}\left(r\frac{n}{K+n}\left(D_2\frac{\partial p_2}{\partial r} - \chi_2 p_2\frac{\partial n}{\partial r}\right)\right) + \ln 2\frac{n}{K+n}\mu_2 p_2$$

$$\frac{\partial n}{\partial t} = r^{-1}\frac{\partial}{\partial r}\left(rD_n\frac{\partial n}{\partial r}\right) - \ln 2\frac{n}{K+n}(\mu_1 p_1 + \mu_2 p_2)$$

which were numerically solved using MATLAB R2013b (MathWorks). For simulations, one-dimensional (Cartesian) and three-dimensional (spherical symmetry) spatial differential operators were adjusted accordingly. Reported values of Monod coefficients, K, are approximately three orders of magnitude lower than the typical nutrient concentration[51]. Hence, we set K to 10^{-3} AU, that is, three orders of magnitude below the initial nutrient concentration ($n(t=0) = 1$ AU). The diffusion coefficient of the nutrient, D_n, is set to 1.8 mm^2 h^{-1}, a value typically used for small molecules in aqueous solutions[52]. Growth rates, $\mu_{1,2}$, are taken from bulk measurements. The active-diffusion coefficients, $D_{1,2}$, were tuned to match the observed expansion rates of the non-chemotactic strains LAB3, LAB4 and LAB5, when grown on soft-agar plates in monoculture. Simulated colony fronts were tracked by following the position at which the cell-density profile crossed a threshold of 0.0125 AU. The chemotactic sensitivity coefficient, $\chi_{1,2}$, is zero for these populations as they do not possess sensing capabilities. For the chemotactic species LAB1, LAB2, A and B, we assumed D to be approximately in the range of the diffusion coefficient of LAB3, LAB4 and LAB5. Subsequently χ was tuned to match their observed expansion rates when grown on soft-agar plates in monoculture.

The initial nutrient profiles were assumed to be flat ($n(t=0) = 1$ AU for all r), while the initial bacterial populations were modelled as a plateau of height p_{initial} and radius r_{plateau} ($r_{\text{plateau}} = 1$ mm, if not noted otherwise) and an adjacent exponentially decaying tail $p_{\text{initial}}e^{-\lambda(r-r_{\text{plateau}})}$. We assume a sharp boundary at the edge of the inoculum as the initial bacterial populations were locally inoculated by pipetting and set λ to 10 mm^{-1}, on the order of several tens of the length of a single bacterium. The total initial population size, $p_{\text{initial},1} + p_{\text{initial},2}$, was set to 10^{-3} AU to match the experimental initial densities used in competition experiments on soft-agar plates, if not noted otherwise. The habitat radius (L) was set to 17.5 mm, matching the radius of the Petri dishes used in experiments, if not noted otherwise. Simulated time (T) was set to 4 days, if not noted otherwise.

We modified the motility terms in the Keller–Segel equations with a Monod-like factor, $\frac{n}{K+n}$, to account for the energy dependence of the active movement of the bacterial populations. Omitting this factor has only mild effects on the final population ratio, whereas the final spatial population profile is substantially altered as profiles flatten out due to active diffusion. We did not observe such flattening out of bacterial profiles experimentally.

Numerical determination of stability and coexistence phase diagram

Stability of community structure (coexistence or extinction of one of the two subpopulations) as shown in Fig. 4c–e and Extended Data Fig. 6b–d was obtained by numerically propagating MKS simulations for initial population ratios (R_0) of 10^{-5} and 10^5 for 7–28 days of simulated time (T). Final population ratios (R_1) were extracted from the last time point. In all cases, the total amount of nutrient had dropped at least to six orders of magnitude below its initial amount, that is, the nutrient was depleted. Community structures were quantified as coexistence (fold change larger than unity for $R_0 = 10^{-5}$ and fold change smaller than unity for $R_0 = 10^5$, grey or white area), extinction of Y (fold change larger than unity for both initial ratios, red area) and extinction of strain X (fold change smaller than unity for both initial ratios, blue area).

Furthermore, we calculated min(abs($\log_{10}(R_1(R_0 = 10^{-5})/10^{-5})$), abs($\log_{10}(R_1(R_0 = 10^5)/10^5)$)) as a quantitative proxy for stability, that is, the shortest log-distance to the zero-fold change line. These quantitative stability values are represented by colour gradients in Fig. 4e (lighter colours correspond to lower stability). Growth and motility parameters of one population were varied as indicated on in the graphs (Fig. 4e and Extended Data Fig. 6b–d) while all strain parameters of the competitor (LAB1 in Fig. 4e and Extended Data Fig. 6b, d, LAB3 in Extended Data Fig. 6c) were kept fixed. $D_X = 0.02$ mm^2 h^{-1} in Extended Data Fig. 6b; $\chi_X = 0$ mm^2 (h (AU))$^{-1}$ in Fig. 4e and Extended Data Fig. 6c, d.

Well-stirred competition model

Competition in the well-stirred culture was modelled as Monod growth on a single limiting nutrient, n.

$$\frac{\partial p_1}{\partial t} = \ln 2 \frac{n}{K+n} \mu_1 p_1$$

$$\frac{\partial p_2}{\partial t} = \ln 2 \frac{n}{K+n} \mu_2 p_2$$

$$\frac{\partial n}{\partial t} = -\ln 2 \frac{n}{K+n} (\mu_1 p_1 + \mu_2 p_2)$$

Model parameters as defined above (MKS model). Equations were numerically solved using MATLAB R2013b.

Strain-specific model parameters

Strain-specific model parameters are described in Supplementary Table 1.

General model parameters

General model parameters are described in Supplementary Table 2.

Plasmids

Plasmids are described in Supplementary Table 3.

Strains

The strains are described in Supplementary Table 4.

E. coli strain RP437 was a gift from H. C. Berg[53]. *E. coli* strain RP437 Δ*cheY* was a gift from V. Sourjik[54]. The *Salmonella typhimurium* strain LT2 (strain number SGSC1412) was obtained from the *Salmonella* Genetic Stock Center (SGSC)[55]. Initially, the strain LT2 was cured of its native pSLT plasmid using the plasmid displacement kit provided by SGSC to yield the cured strain. All deletions were constructed by allele replacement using lambda red recombinase. *E. coli* ECOR strains were obtained from the STEC Center[22]. *E. coli* strain UU2612 was a gift from J. S. Parkinson[56].

pTrc99A carries a pBr origin of replication, ampicillin antibiotic resistance and an IPTG-inducible induction system. pKG116 carries a pACYC origin of replication, chloramphenicol antibiotic resistance and a salicylate-inducible induction system.

Statistics and reproducibility

Tile-scan fluorescence imaging. For each experiment, cells were prepared as described above. The total number of times (n) each experiment was performed on cells from m independent overnight cultures is included as 'figure panel, strain combination or condition = n/m': Fig. 2a, A = 5/3, B = 4/3, A and B = 17/3; Fig. 2b, all strains = 2/1; Fig. 2c, LAB1 = 10/7, LAB2 = 6/4, LAB1 and LAB2 = 24/3; Fig. 2d, LAB3 = 9/7, LAB4 = 5/4, LAB3 and LAB4 = 34/4; Fig. 2e, LAB3 = 9/7, LAB2 = 6/4, LAB3 and LAB2 = 7/3; Fig. 2f, LAB1 = 10/7, LAB5 = 4/2, LAB1 and LAB5 = 6/2; Fig. 3a, A = 3/2, B = 3/2, A and B = 2/1; Fig. 3c, A = 3/2, B = 3/2, A and B = 2/1; Fig. 3d, A = 3/2, B = 3/2, A and B = 2/1; Fig. 3e, A and B ($R = 10^0$) = 17/4, A and B ($R = 10^{-1}, 10^1$) = 3/1, A and B ($R = 10^{-2}, 10^2$) = 7/2, LAB1 and LAB5 = 3/1; Extended Data Fig. 1g, ECOR36 = 2/1, ECOR8 = 2/1, ECOR36 and ECOR8 = 3/1, ECOR68 = 2/2, ECOR32 = 2/2, ECOR68 and ECOR32 = 3/2, ECOR18 = 2/2, ECOR19 = 2/2, ECOR18 and ECOR19 = 3/2, ECOR21 = 2/2, ECOR20 = 2/2, ECOR21 and ECOR20 = 3/2, ECOR3 = 2/1, ECOR34 = 2/1, ECOR3 and ECOR34 = 3/1; Extended Data Fig. 3a, edge inoculation = 6/1, centre inoculation = 2/1; Extended Data Fig. 4a, A and A-YFP = 2/1, A and B-CFP = 2/1, A and blank = 2/1, blank and A-YFP = 2/1, blank and B-CFP = 2/1, blank and blank = 2/1, B and A-YFP = 2/1, B and B-CFP = 2/1, B and blank = 2/1, tet and A-YFP = 2/1, tet and B-CFP = 2/1, tet and blank = 2/1; Extended Data Fig. 7k–m overlapping inoculation = 3/3, close by inoculation = 3/3, far apart inoculation = 3/3. All replicates showed similar results. Representative images and data are shown.

Bacterial growth measurements. For each experiment, cells were prepared as described above. The total number of times (n) each experiment was performed on cells from m independent overnight cultures is included as 'figure panel, strain = n/m': Fig. 2b, all strains = 2/1; Fig. 2g, LAB1 = 44/3, LAB2 = 23/2, LAB3 = 20/2, LAB4 = 12/1, LAB5 = 21/1; Extended Data Fig. 1f, same data as Fig. 2b; Extended Data Fig. 8b, same data as Fig. 2b; Extended Data Fig. 9b both strains = 9/3. In Fig. 2b, open circles indicate measurements on different samples from the same overnight culture, filled circles indicate means across all samples. In Fig. 2g, open circles indicate means of all measurements from each independent overnight culture, filled circles indicate means across all overnight cultures. In Extended Data Fig. 9b, open circles represent the global mean and error bars indicate the standard error of the mean across independent overnight cultures.

Migration (colony expansion) rate measurements. For each experiment, cells were prepared as described above. The total number of times (n) each experiment was performed on cells from m independent overnight cultures is included as 'figure panel, strain combination or condition = n/m': Fig. 2b, all strains = 2/1; Fig. 2g, LAB1 = 6/5, LAB2 = 2/2, LAB3 = 4/4, LAB4 = 2/2, LAB5 = 2/1; Extended Data Fig. 8a, same data as Fig. 2b; Extended Data Fig. 9d, TSS1410 0 μM IPTG = 2/2, TSS1410 2.5 μM IPTG = 3/3, TSS1410 5 μM IPTG = 3/3, TSS1410 10 μM IPTG = 4/4, TSS1410 25 μM IPTG = 3/3, TSS1410 50 μM IPTG = 3/3, TSS1410 100 μM IPTG = 3/3, TSS1410 200 μM IPTG = 2/2, TSS1709 0 μM IPTG = 2/2, TSS1709 2.5 μM IPTG = 3/3, TSS1709 5 μM IPTG = 3/3, TSS1709 10 μM IPTG = 4/4, TSS1709 25 μM IPTG = 3/3, TSS1709 50 μM IPTG = 3/3, TSS1709 100 μM IPTG = 3/3, TSS1709 200 μM IPTG = 2/2. In Fig. 2b, open circles indicate measurements on different samples from the same overnight culture, filled circles indicate means across all samples. In Fig. 2g, open circles indicate measurements on different samples from the same or independent overnight cultures, filled circles indicate means across all samples. In Extended Data Fig. 9d, large open circles represent the mean and error bars indicate the standard error of the mean across independent overnight cultures.

Swimming speed measurements. For each experiment, cells were prepared as described above. The total number of times (n) a recording was acquired on cells from m independent overnight cultures is included as 'figure panel, strain combination or condition = n/m': Extended Data Fig. 8a, b, ECOR18 = 4/1, ECOR19 = 5/2, ECOR20 = 5/2, ECOR21 = 6/2, ECOR3 = 2/2, ECOR34 = 3/2, ECOR68 = 4/2, ECOR32 = 4/2, ECOR8 = 4/2, ECOR36 = 2/2. Open circles indicate measurements from two independent overnight cultures. Filled circles indicate weighted-means across all acquisitions (with the error estimate weights). The error bars indicate the standard error of the weighted mean, corrected for overdispersion; Extended Data Fig. 9c, TSS1410 0 μM IPTG = 2/2, TSS1410 5 μM IPTG = 4/2, TSS1410 10 μM IPTG = 4/2, TSS1410 25 μM IPTG = 2/2, TSS1410 50 μM IPTG = 2/2, TSS1410 100 μM IPTG = 4/2, TSS1410 200 μM IPTG = 2/1, TSS1709 0 μM IPTG = 2/2, TSS1709 5 μM IPTG = 3/2, TSS1709 10 μM IPTG = 3/2, TSS1709 25 μM IPTG = 2/2, TSS1709 50 μM IPTG = 2/1, TSS1709 100 μM IPTG = 2/1. For Extended Data Fig. 9c, variation between recordings from different overnight cultures was not noticeably larger than variation between recordings from the same repeat, thus the mean for each condition was determined as the error-weighted mean across all recordings. The error bar given is the standard error of the weighted mean, corrected for overdispersion.

Flagellar staining experiments. For each experiment, cells were prepared as described above. Staining of the flagella was performed once for each IPTG concentration. However, similar results to the shown data for TSS1410 at 10 μM IPTG were obtained independently at 5 μM,

and similar results to the shown images for TSS1410 at 100 µM were obtained independently at 50 µM. TSS1709 showed similar results at 10, 50 and 100 µM IPTG.

Soft-agar migration phenotyping. For each experiment, cells were prepared as described above. Images shown in Extended Data Fig. 3b were recorded once. Images shown in Extended Data Fig. 9e are representative, repeats gave similar results. Repeats differed in the number of strains and IPTG conditions included.

Fold change measurements. For each experiment, cells were prepared as described above. Data of Fig. 1b, c are replotted in Fig. 3f, for comparison. Data obtained from representative overnight cultures are shown, except for the open bars in Fig. 4f–h, which show the means of data shown in Fig. 3f, and solid bars in Extended Data Fig. 1a–e, which show the means over all replicates. The total number of times (n) each experiment was performed on cells from m independent overnight cultures, is included as 'figure panel, strain combination or condition = n/m': Fig. 1b, ECOR18 and ECOR19 (liquid, colony counting, $R_0 = 10^0$) = 3/2, ECOR18 and ECOR19 (liquid, colony counting, $R_0 = 10^{-2}$ and $R_0 = 10^2$) = 2/2; Fig. 1c, ECOR18 and ECOR19 (plate, colony counting, $R_0 = 10^0$) = 2/1, ECOR18 and ECOR19 (plate, colony counting, $R_0 = 10^{-2}$ and $R_0 = 10^2$) = 2/2; Fig. 3f, ECOR18 and ECOR19 (plate, tile-scan microscopy, $R = 10^0$) = 17/4, ECOR18 and ECOR19 (plate, tile-scan microscopy, $R = 10^{-1}$ and 10^1) = 3/1, ECOR18 and ECOR19 (plate, tile-scan microscopy, $R = 10^{-2}$ and 10^2) = 7/2, LAB5 and LAB1 (plate, tile-scan microscopy, all ratios) = 6/2; Fig. 4f, LAB5 and LAB1 (open bars, spot inoculation) = 6/2, LAB5 and LAB1 (closed bars, spread-out inoculation) = 3/1; Fig. 4g, LAB5 and LAB1 (open bars) show the same data as in Fig. 4f, LAB5 and LAB1 (closed bars, pelleted inoculation) = 3/1; Fig. 4h, LAB5 and LAB1 (open bars) show same data as in Fig. 4f, LAB3 and LAB2 (closed bars, spot inoculation) = 2/1; Extended Data Fig. 1a–e, ECOR18 and ECOR19 = 6/2, ECOR32 and ECOR68 = 6/2, ECOR36 and ECOR8 = 3/1, ECOR3 and ECOR34 = 3/1, ECOR20 and ECOR21 = 6/2; Extended Data Fig. 7k–m, LAB3 and LAB2 (overlapping) = 3/3, LAB3 and LAB2 (close by inoculation) = 3/3, LAB3 and LAB2 (far apart inoculation) = 3/3. All replicates showed similar results.

Reporting summary

Further information on research design is available in the Nature Research Reporting Summary linked to this paper.

Data availability

The data that support the findings of this study are available from the corresponding authors upon reasonable request.

Code availability

Custom-written scripts used in this study are available from the corresponding authors upon reasonable request.

35. Taute, K. M., Gude, S., Tans, S. J. & Shimizu, T. S. High-throughput 3D tracking of bacteria on a standard phase contrast microscope. *Nat. Commun.* **6**, 8776 (2015).
36. Berg, H. C. & Brown, D. A. Chemotaxis in *Escherichia coli* analyzed by three-dimensional tracking. *Antibiot. Chemother.* **19**, 55–78 (1974).
37. Boyd, S., Parikh, N., Chu, E., Peleato, B. & Eckstein, J. Distributed optimization and statistical learning via the alternative direction method of multipliers. *Found. Trends Mach. Learn.* **3**, 1–122 (2011).
38. Leifson, E. Staining, shape and arrangement of bacterial flagella. *J. Bacteriol.* **62**, 377–389 (1951).
39. Schneider, C. A., Rasband, W. S., & Eliceiri, K. W. NIH Image to ImageJ: 25 years of image analysis. *Nat. Methods* **9**, 671–675 (2012).
40. Edelstein, A. D. et al. Advanced methods of microscope control using μManager software. *J. Biol. Methods* **1**, e10 (2014).
41. Leinonen, R., Sugawara, H., Shumway, M. & The International Nucleotide Sequence Database Collaboration. The Sequence Read Archive. *Nucleic Acids Res.* **39**, D19–D21 (2010).
42. Joshi, N. A. & Fass, J. N. Sickle: a sliding-window, adaptive, quality-based trimming tool for FastQ files. v.1.33 https://github.com/najoshi/sickle (2011).
43. Langmead, B. & Salzberg, S. L. Fast gapped-read alignment with Bowtie 2. *Nat. Methods* **9**, 357–359 (2012).
44. McKenna, A. et al. The Genome Analysis Toolkit: a MapReduce framework for analyzing next-generation DNA sequencing data. *Genome Res.* **20**, 1297–1303 (2010).
45. Cingolani, P. et al. Using *Drosophila melanogaster* as a model for genotoxic chemical mutational studies with a new program, SnpSift. *Front. Genet.* **3**, 35 (2012).
46. Danecek, P. et al. The variant call format and VCFtools. *Bioinformatics* **27**, 2156–2158 (2011).
47. Cingolani, P. et al. A program for annotating and predicting the effects of single nucleotide polymorphisms, SnpEff: SNPs in the genome of *Drosophila melanogaster* strain *w1118; iso-2; iso-3*. *Fly* **6**, 80–92 (2012).
48. Python Software Foundation. Python v.3.6.7 http://www.python.org (2018).
49. Cock, P. J. et al. Biopython: freely available Python tools for computational molecular biology and bioinformatics. *Bioinformatics* **25**, 1422–1423 (2009).
50. Monod, J. The growth of bacterial cultures. *Annu. Rev. Microbiol.* **3**, 371–394 (1949).
51. Senn, H., Lendenmann, U., Snozzi, M., Hamer, G. & Egli, T. The growth of *Escherichia coli* in glucose-limited chemostat cultures: a re-examination of the kinetics. *Biochim. Biophys. Acta* **1201**, 424–436 (1994).
52. Hazel, J. R. & Sidell, B. D. A method for the determination of diffusion coefficients for small molecules in aqueous solution. *Anal. Biochem.* **166**, 335–341 (1987).
53. Parkinson, J. S. Complementation analysis and deletion mapping of *Escherichia coli* mutants defective in chemotaxis. *J. Bacteriol.* **135**, 45–53 (1978).
54. Sourjik, V. & Berg, H. C. Localization of components of the chemotaxis machinery of *Escherichia coli* using fluorescent protein fusions. *Mol. Microbiol.* **37**, 740–751 (2000).
55. Zinder, N. D. & Lederberg, J. Genetic exchange in *Salmonella*. *J. Bacteriol.* **64**, 679–699 (1952).
56. Zhou, Q., Ames, P., & Parkinson, J. S. Biphasic control logic of HAMP domain signalling in the *Escherichia coli* serine chemoreceptor. *Mol. Microbiol.* **80**, 596–611 (2011).
57. Turner, L., Ryu, W. S. & Berg, H. C. Real-time imaging of fluorescent flagellar filaments. *J. Bacteriol.* **182**, 2793–2801 (2000).
58. Yamashita, I. et al. Structure and switching of bacterial flagellar filaments studied by X-ray fiber diffraction. *Nat. Struct. Biol.* **5**, 125–132 (1998).
59. Lynch, M. & Marinov, G. K. The bioenergetic costs of a gene. *Proc. Natl Acad. Sci. USA* **112**, 15690–15695 (2015).
60. Tran, Q. H. & Unden, G. Changes in the proton potential and the cellular energetics of *Escherichia coli* during growth by aerobic and anaerobic respiration or by fermentation. *Eur. J. Biochem.* **251**, 538–543 (1998).
61. Ryu, W. S., Berry, R. M. & Berg, H. C. Torque-generating units of the flagellar motor of *Escherichia coli* have a high duty ratio. *Nature* **403**, 444–447 (2000).
62. Bremer, H. & Dennis, P. P. in *Escherichia coli and Salmonella: Cellular and Molecular Biology* (ed. Neidhardt, F. C.) **Ch. 97** (ASM, 1996).

Acknowledgements Work in the groups of S.J.T. and T.S.S. is supported by the Netherlands Organization for Scientific Research (NWO). T.S.S. also acknowledges partial support by the Allen Distinguished Investigator Program (grant 11562) through the Paul G. Allen Frontiers Group. We thank H. C. Berg, J. S. Parkinson and V. Sourjik for providing strains and plasmids, V. Sunderlikova, S. Verstege-Boskamp and Z. Stachova Rychnavskafor for technical assistance, M. Lazova for early ECOR strain experiments, T. Averink and N. Anand for help with plasmid construction, F. Büke for his help with the plate-reader measurements, M. Akman for help with genomics analyses and P. R. ten Wolde, J. van Zon and S. Werner for reading the manuscript.

Author contributions S.G., K.M.T., T.S.S. and S.J.T. conceived the research. S.G., E.P., K.M.T., T.S.S. and S.J.T. designed the experiments. S.G., E.P. and A.-B.S. performed the competition experiments, S.G. performed the LAB strain characterizations, E.P. and S.G. performed the wild isolate characterization, E.P. performed the wild isolate three-dimensional tracking, S.G. and E.P. performed the fluorescence calibration measurements, S.G performed the secreted compound tests, K.M.T performed the motility cost and corresponding trade-off experiments. S.G., E.P. and K.M.T. analysed the data, S.G. performed the numerical simulations and sequence analysis. S.G., E.P., K.M.T., T.S.S. and S.J.T. contributed to writing the manuscript.

Competing interests The authors declare no competing interests.

Additional information

Supplementary information is available for this paper at https://doi.org/10.1038/s41586-020-2033-2.

Correspondence and requests for materials should be addressed to T.S.S. or S.J.T.

Peer review information *Nature* thanks Jeff Gore and the other, anonymous, reviewer(s) for their contribution to the peer review of this work.

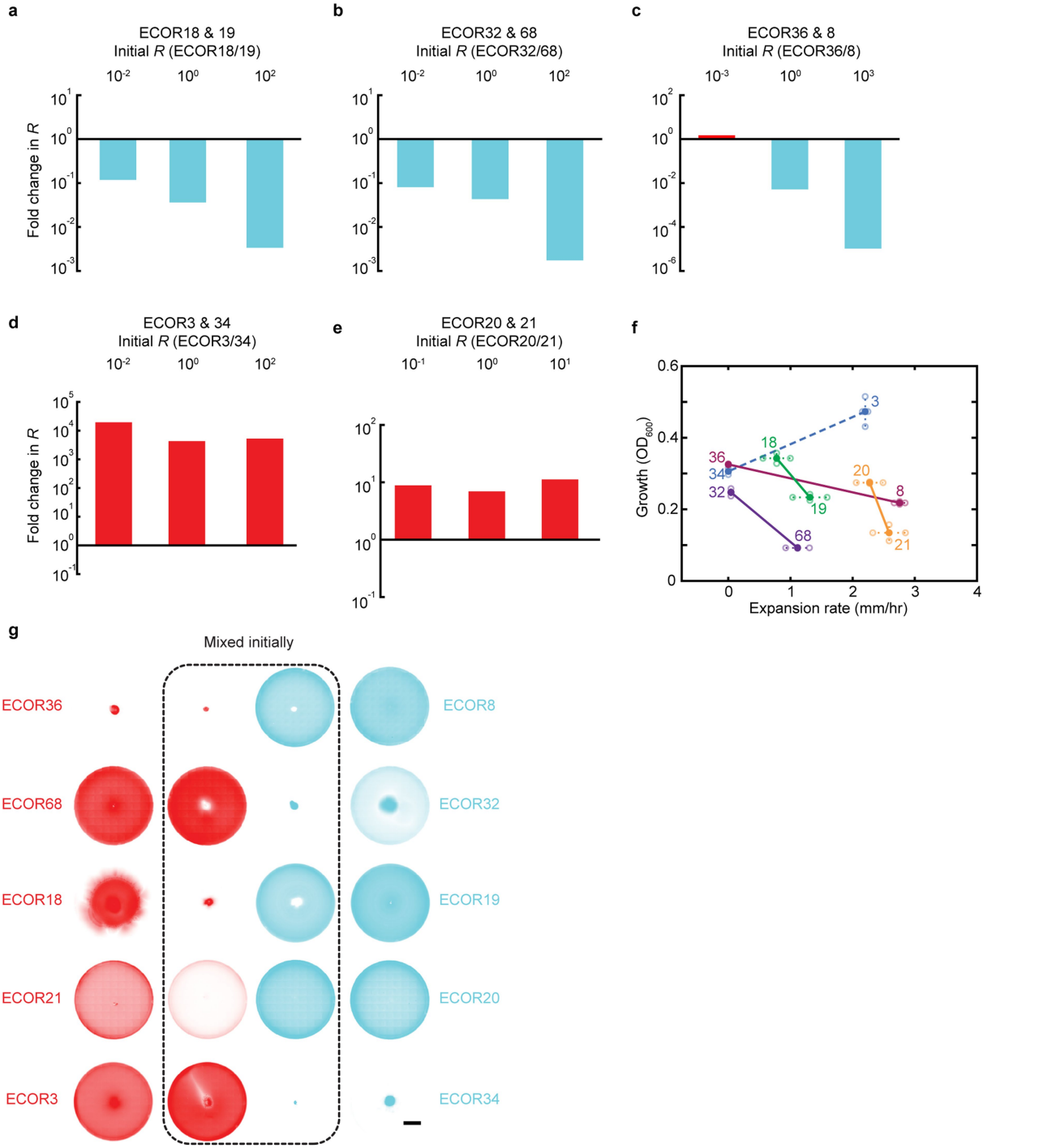

Extended Data Fig. 1 | Competition and selection functions of cohabitant wild isolate strains. a–**e**, Fold change of the population ratio R as a function of initial R_0 for the five cohabitant pairs of the ECOR strain collection that could be transformed with plasmids for expression of fluorescent-protein labels. Out of the five pairs, three (ECOR18(A)–ECOR19(B) (**a**), ECOR32–ECOR68 (**b**) and ECOR36–ECOR8 (**c**)) clearly demonstrated a negative selection function, and one pair (ECOR36–ECOR8 (**b**)) showed, in addition, hierarchy inversion. The competition experiments were performed in TB soft-agar assays (see Methods). **f**, Scatter plot of growth propensity (OD_{600} at 7.5 h of growth in 96-well plate) versus migration rate for the five tested cohabitant pairs (same data as in Fig. 2b, reproduced here for convenience). **g**, Reciprocal spatial exclusion observed in cohabitant pairs of wild isolate strains. Tiled fluorescence micrographs show that out of the five cohabitant pairs tested, three (ECOR8–ECOR36, ECOR68–ECOR32 and ECOR18(A)–ECOR19(B)) exhibit spontaneous segregation into proximal and distal territories. The pairs were co-cultured in TB-based soft-agar gels with identical dimensions as plates shown at Fig. 2a, c–f (approximately 4 mm high, 35 mm in diameter). Scale bar, 7.5 mm.

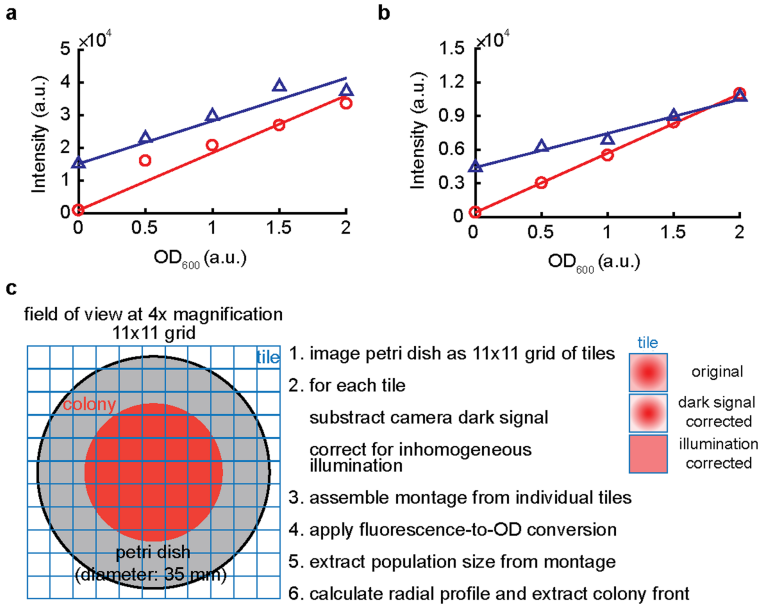

Extended Data Fig. 2 | Calibrated tile-scan fluorescence microscopy. **a**, **b**, Calibration curves relating cell density (in OD_{600} (AU)) to fluorescence intensity was obtained by imaging soft-agar plates into which different known densities of cells were suspended in the molten agar before cooling to form the gel (see Methods). Calibration curves for TB (ECOR18(eYFP) (red) and ECOR19(eCFP) (blue)) (**a**) and MMH1 (LAB1(eYFP) (red) and LAB5(eCFP) (blue)) (**b**). Similar calibration curves were obtained for LAB1(eYFP) and LAB2(eCFP) in MMH1. **c**, Calibrated tile-scan fluorescence microscopy. Petri dishes (35 mm diameter) containing soft-agar gel medium were imaged by scanning an 11 × 11 grid of image fields (tiles) for each channel (YFP, CFP and bright field) at each time point. Image post-processing was performed for each tile individually. Subsequently, tile images were assembled into montages. Montages were converted and population size and colony front position were extracted.

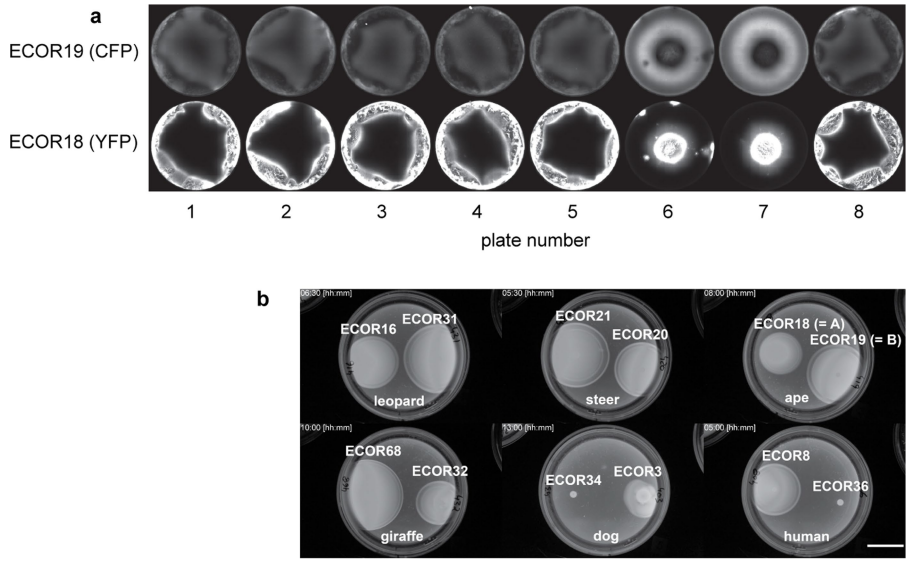

Extended Data Fig. 3 | Edge inoculation in minimal medium and colony expansion in rich medium. a, Reciprocal spatial exclusion was confirmed in both centre- and edge-inoculated competitions in the soft-agar gel environment. ECOR18 and ECOR19 labelled with YFP and CFP, respectively (strains A and B in the main text) were pre-grown on TB and glycerol minimal medium as described in the Methods. The OD_{600} of both strains was adjusted to 10^{-2}. Strains were mixed 1:1 and subsequently mixed with twofold concentrated molten agar. The final mixture was kept at room temperature for 1.5 h to transition into a gel state. The gel, containing a mixture of ECOR18 and ECOR19, was transferred onto soft-agar plates using a 1-ml pipette, either around the edge of the plate (plates 1–5 and 8) or into the centre (plates 6 and 7). All eight plates were placed at 33.5 °C in a humid environment for approximately 4 days and subsequently imaged by fluorescence microscopy. When inoculated around the edge, ECOR18 occupies the edge region, while ECOR19 is seen closer to the centre of the dish. Conversely, when inoculated in the centre ECOR18 occupies the central region of the dish, while ECOR19 is seen further away from the centre. Hence, spatial exclusion is seen for both centre and edge inoculation. Petri dish diameter: 35 mm. **b**, Migration phenotypes of all six cohabitant pairs (that is, isolated from the same host) in the ECOR strain collection on LB soft-agar plates at 37 °C. Petri dish diameter: 90 mm. The images of culture plates were acquired at different time points (see top-left inset of each sub-image). Scale bar, 25 mm.

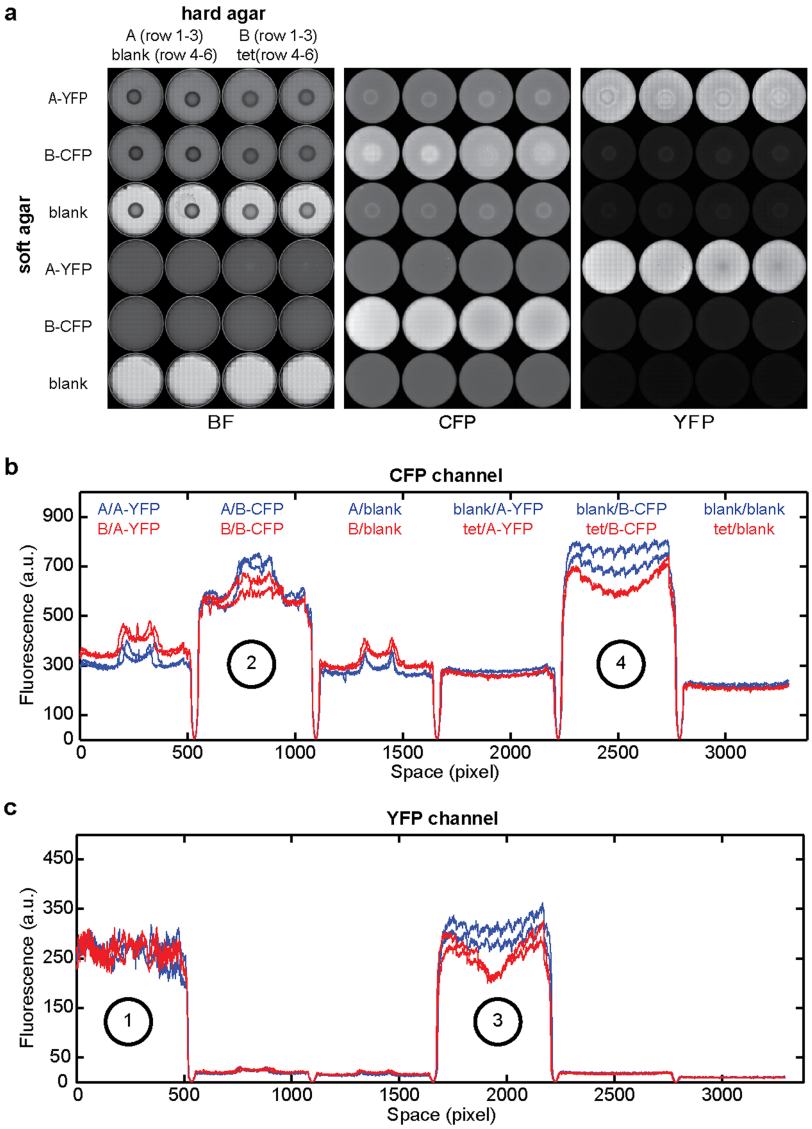

Extended Data Fig. 4 | Test for secreted compounds that inhibit growth. **a**, Tile-scanned snapshots of Petri dishes (diameter 35 mm) in bright-field (BF) and fluorescence (CFP and YFP) after approximately 3 days. Images were not corrected for background or autofluorescence of the cells. TB hard-agar plates (1.5% (w/v)) were prepared in four different ways; either pre-inoculated with a drop of 10 µl saturated TB culture of unlabelled A or B, left empty (blanks), or addition of a drop of 10 µl tetracycline (5 mM) after 2 days (tet). Plates inoculated with A or B were placed at 33.5 °C in a humid environment for 2 days. Plates not pre-inoculated with A or B were stored at 4 °C. Subsequently all gels were covered with a layer of TB soft agar (0.26% (w/v)) containing diluted, saturated cultures of either A (labelled with YFP, A-YFP), B (labelled with CFP, B-CFP) or neither of the two (blank). The soft-agar gel contained the necessary antibiotics and inducers (see Methods). All plates were placed on 33.5 °C in a humid environment for 18 h and were then imaged. **b**, **c**, Fluorescence intensities extracted along vertical lines through the snapshots shown in **a**, for the CFP channel (**b**) and YFP channel (**c**). Lines were manually centred on the colonies of A and B as seen in the bright-field image. Each group indicates the hard agar/soft agar combinations. For example, A/A-YFP indicates a TB hard-agar gel pre-inoculated with unlabelled A, covered with TB soft-agar gel containing A (labelled with YFP). The presence of pre-grown B does not negatively affect the growth of A-YFP as its profile is indistinguishable from the profile of A-YFP when grown in the presence of pre-grown A (**c**, marker 1). The presence of tetracycline affects the growth of A-YFP negatively, as is clearly indicated by the central dip in its profile compared to the blank (**c**, marker 3). In the same way, the presence of pre-grown A does not negatively affect the growth of B-CFP as its profile shows higher rather than lower intensities compared to the profile of B-CFP when grown in the presence of pre-grown B (**b**, marker 2). The presence of tetracycline affects the growth of B-CFP negatively, as is indicated by the central dip in its profile compared to the blank (**b**, marker 4). Hence, we do not observe evidence that either A or B secretes growth-inhibitory compounds such as antibiotics or toxins.

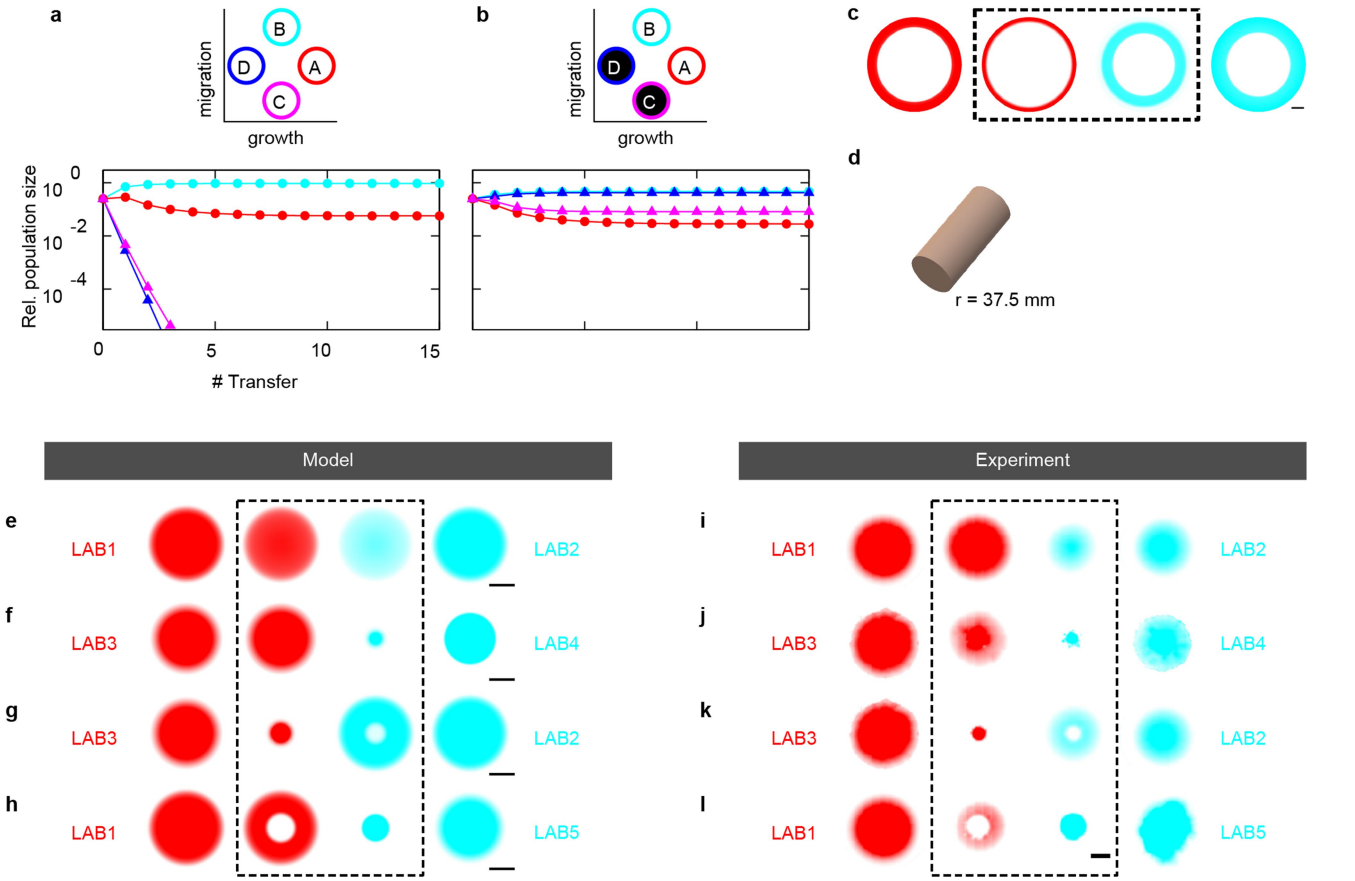

Extended Data Fig. 5 | Additional strains and simulation-experiment comparison. a, **b**, Simulations of repeated competitive migration into a virgin nutrient patch. Top, growth and migration phenotypes of the strains are schematically illustrated. Bottom, each point is one round of competitive migration into a virgin nutrient patch. Resulting population ratios are the starting point for the next round. The populations thus can spatially segregate during rounds, and are re-mixed in between rounds. Relative population sizes are indicated as a function of a round number. **a**, Four populations and one common nutrient. The A–B pair (not to be confused with the strains A and B in the main text) exhibits a growth–migration trade-off and coexists (data not shown). In the presence of two additional strains, C and D, we find that the coexistence of A–B is not broken. Not all four populations coexist, as C and D become extinct. Parameters: population A (red, $\mu = 0.8$ dbl h^{-1}, $v = 0.55$ mm h^{-1}, $\chi = 1.15$ mm^2 (h (AU))$^{-1}$, $D = 0.02$ mm^2 h^{-1}), population B (light blue, $\mu = 0.6$ dbl h^{-1}, $v = 0.8$ mm h^{-1}, $\chi = 2.25$ mm^2 (h (AU))$^{-1}$, $D = 0.02$ mm^2 h^{-1}), population C (magenta, $\mu = 0.6$ dbl h^{-1}, $v = 0.3$ mm h^{-1}, $\chi = 0.55$ mm^2 (h (AU))$^{-1}$, $D = 0.02$ mm^2 h^{-1}) and population D (dark blue, $\mu = 0.4$ dbl h^{-1}, $v = 0.55$ mm h^{-1}, $\chi = 2.0$ mm^2 (h (AU))$^{-1}$, $D = 0.02$ mm^2 h^{-1}). **b**, The same four populations, but now A–B and C–D have their own metabolic niche, as they consume different nutrients. All four strains adopt a stable equilibrium value, illustrating how multiple coexistence mechanisms can work together to stabilize complex communities. Populations were transferred as 1/25,000 dilutions into habitats with replenished nutrients after 4 days. Nutrients are exhausted at all transfers. Habitat size: 17.5 mm. Simulation performed using the MKS model with parameters as described in the Methods. **c**, **d**, Simulations of ECOR18 and ECOR19 in gut dimensions. **c**, Simulations of ECOR18 (red) and ECOR19 (blue) alone (leftmost and rightmost images, respectively) and as mixed population at initial ratio of 1 (two middle images). Spatial patterns are reported after 40 h in cylindrical habitats of radius 37.5 mm and edge inoculation. Scale bar, 10 mm. Simulation performed using the MKS model with parameters as described in the Methods. **d**, Illustration of the cylindrical habitat. **e**–**l**, Simulations of (**e**–**h**) and experimentally measured (**i**–**l**) spatial patterns of LAB strains as monocultures (leftmost and rightmost images, respectively) and as mixed populations at initial ratio of 1 (two middle images). Experimental data as shown in Fig. 2c–f are repeated here for convenience. Spatial patterns are reported after 4 days in circular habitats of radius 17.5 mm and centre inoculation. Scale bars, 10 mm (**e**–**h**) and 7.5 mm (**i**–**l**). Simulation performed using MKS model with parameters as described in the Methods.

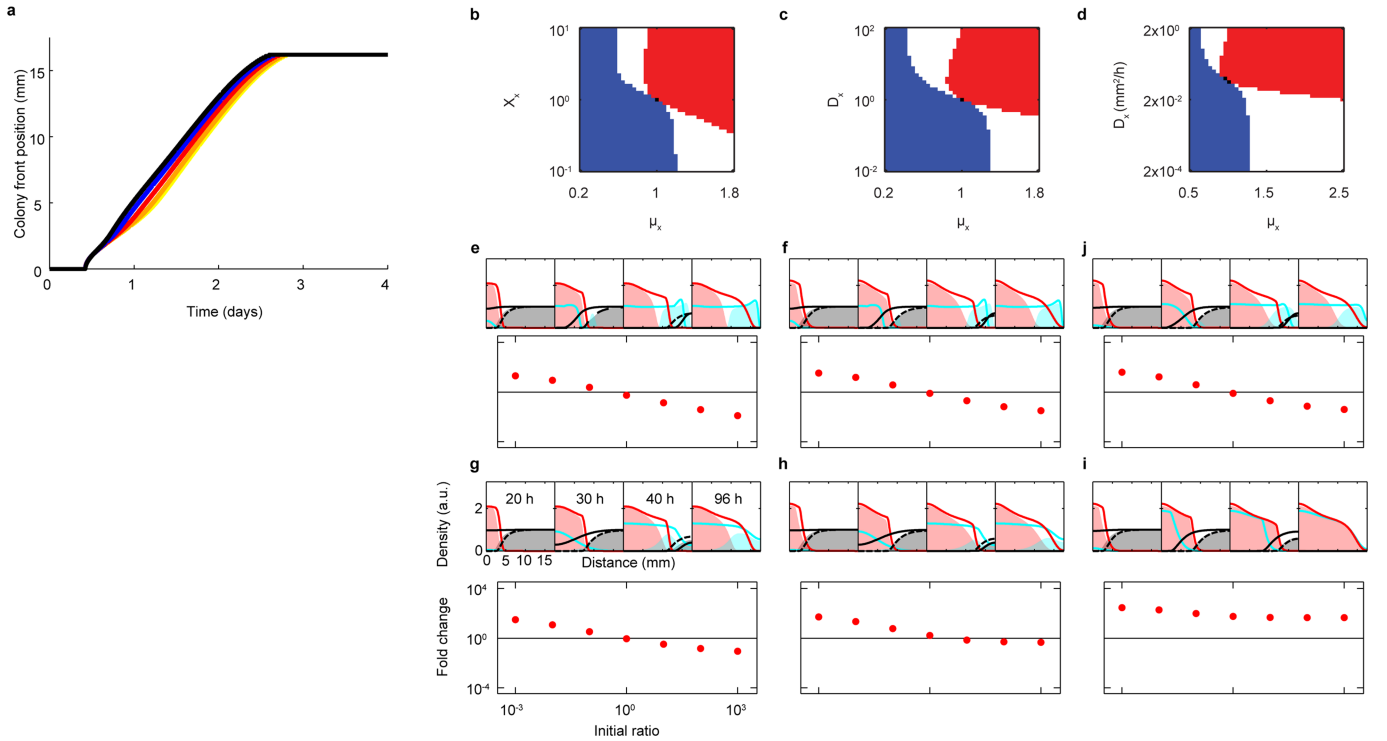

Extended Data Fig. 6 | Different modes of motility can support coexistence. **a**, Departure of fast movers depends on growth rate of slow mover. Simulated colony front position of fast movers versus time, for different growth rates of slow movers (yellow to black: $\mu_S = 0.4, 0.5, 0.6, 0.7, 0.8$ dbl h^{-1}. Parameters for slow movers: $D_S = 0.02$ mm^2 h^{-1}, $\chi_S = 0$ mm^2 (h (AU))$^{-1}$. Fast movers: $\mu_F = 0.5$ dbl h^{-1}, $D_F = 0.02$ mm^2 h^{-1}, $\chi_F = 0.875$ mm^2 (h (AU))$^{-1}$. Habitat radius: 17.5 mm. Simulations were performed using the MKS model with parameters as described in the Methods. **b**–**d**, Phase diagrams show the coexistence for chemotactic and non-chemotactic strains. Parameters are fixed for strain Y, and varied for strain X: growth rate μ_X (in units of μ_Y), diffusive mobility D_X (**c**, in units of D_Y; **d**, in mm^2 h^{-1}) and chemotactic coefficient χ_X (in units of χ_Y). Blue, Y excludes X (X has low growth and motility). Red, X excludes Y (X has high growth and motility). White, stable coexistence (trade-off, with X faster grower in bottom right, X faster mover in top left). Black, unstable coexistence. **b**, Both X and Y are chemotactic (Y = LAB1). **c**, Both X and Y are non-chemotactic (Y = LAB3). **d**, Y is chemotactic, while X is not (Y = LAB1). Same as Fig. 4e. Simulations performed using the MKS model with parameters of indicated reference strains and $D_X = 0.02$ mm^2 h^{-1} in **b**. $\chi_X = 0$ mm^2 (h (AU))$^{-1}$ in **c** and **d**. Habitat size in all panels: 17.5 mm. Simulation performed using MKS model with parameters as described in t he Methods. **e**–**h**, Chemotaxis is not essential for coexistence but does give an advantage. Top, snapshots of spatial density profiles at initial ratio R (fast growers (red), fast movers (blue)) of 1. Bottom, fold change versus initial ratio. Monocultures in solid lines, mixed populations as shaded regions. Chemotactic populations: both (**e**), only fast movers (**f**), only slow movers (**g**), neither of the two (**h**). **e**–**h**, Reciprocal spatial exclusion and coexistence occur, but the details differ. Specifically, when fast movers are chemotactic (**e**, **f**), they form more narrowly distributed travelling waves, spatially exclude slow movers better and increase invasion capacity (for example, at high R the fold change is higher in **e** than **h**). These results indicate a competitive advantage of chemotaxis over active random motion alone. **e**–**h**, Parameters: red fast growers ($\mu = 0.75$ dbl h^{-1}, $v = 0.4$ mm h^{-1}), blue fast movers ($\mu = 0.5$ dbl h^{-1}, $v = 0.8$ mm h^{-1}). **e**, Specific parameters: blue: $\chi = 3$ mm^2 (h (AU))$^{-1}$, $D = 0.02$ mm^2 h^{-1}, red: $\chi = 0.775$ mm^2 (h (AU))$^{-1}$, $D = 0.02$ mm^2 h^{-1}. **f**, Specific parameters: blue: $\chi = 3$ mm^2 (h (AU))$^{-1}$, $D = 0.02$ mm^2 h^{-1}, red: $\chi = 0$ mm^2 (h (AU))$^{-1}$, $D = 0.0775$ mm^2 h^{-1}. **g**, Specific parameters: blue: $\chi = 0$ mm^2 (h (AU))$^{-1}$, $D = 0.365$ mm^2 h^{-1}, red: $\chi = 0.775$ mm^2 (h (AU))$^{-1}$, $D = 0.02$ mm^2 h^{-1}. **h**, Specific parameters: blue: $\chi = 0$ mm^2 (h (AU))$^{-1}$, $D = 0.365$ mm^2 h^{-1}, red: $\chi = 0$ mm^2 (h (AU))$^{-1}$, $D = 0.0775$ mm^2 h^{-1}. Habitat size in all panels: 17.5 mm. Simulation was performed using the MKS model with parameters as described in the Methods. **i**, **j**, A poor competitor (**i**, blue: slow growth, weak random motion without chemotaxis) can become a competitive invader that can coexist with faster growers (red) when it becomes chemotactic (**j**). **i**, Parameters: blue and red are non-chemotactic and have identical expansion rates ($v = 0.4$ mm h^{-1}). Red: $\mu = 0.75$ dbl h^{-1}, $\chi = 0$ mm^2 (h (AU))$^{-1}$, $D = 0.0775$ mm^2 h^{-1}. Blue: $\mu = 0.5$ dbl h^{-1}, $\chi = 0$ mm^2 (h (AU))$^{-1}$, $D = 0.115$ mm^2 h^{-1}. **j**, Parameters: red: $\mu = 0.75$ dbl h^{-1}, $v = 0.4$ mm h^{-1}, $\chi = 0$ mm^2 (h (AU))$^{-1}$, $D = 0.0775$ mm^2 h^{-1}. Blue: $\mu = 0.5$ dbl h^{-1}, $v = 0.8$ mm h^{-1}, $\chi = 2.4$ mm^2 (h (AU))$^{-1}$, $D = 0.115$ mm^2 h^{-1}. Habitat size in all panels: 17.5 mm. Simulation was performed using the MKS model with parameters as described in the Methods.

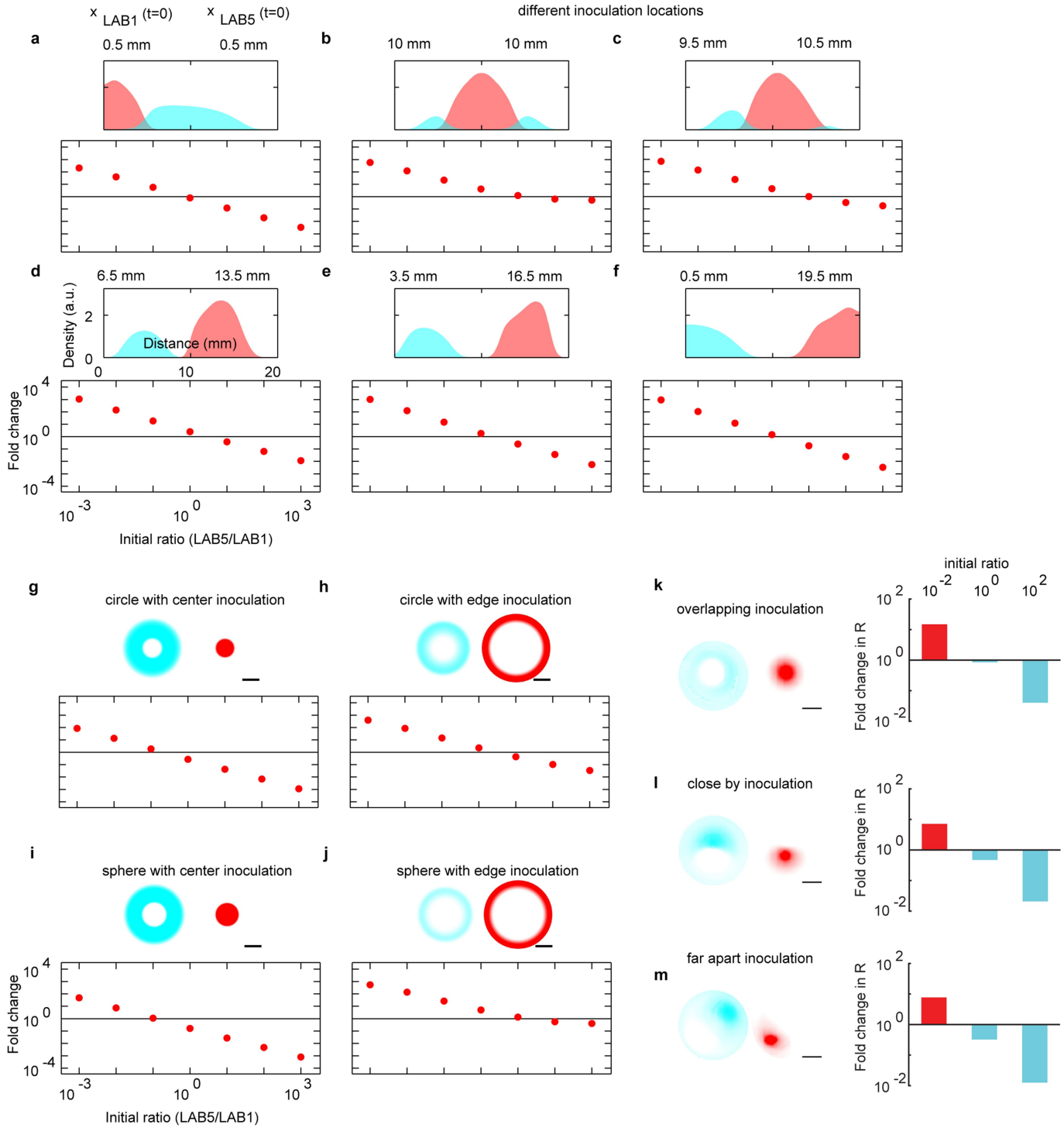

Extended Data Fig. 7 | See next page for caption.

Extended Data Fig. 7 | Coexistence under different inoculation and patch geometries. a–**f**, Inoculation of mixed strain co-culture at the edge (**a**) and centre (**b**) of the patch, and of each strain separately at a distance of 1, 7, 13 and 19 mm relative to the centre (**c**–**f**). Inoculation regions are 1 mm wide, so they are in direct contact in **c**. Simulations are for a linear (one-dimensional) patch geometry. Fast-mover LAB1 (blue) and fast-grower LAB5 (red). Top, spatial pattern for initial ratio (fast grower/fast mover) of 1. Bottom, selection functions. For all cases the selection function crosses a fold change of unity (black line), indicating hierarchy inversion. The stability of coexistence, as assessed by the distance of the selection function from the unity fold change line at low and high initial ratios, is higher for separate inoculations, and increases with inoculation distance (**c**–**f**). These findings indicate that separated inoculation corresponds to having (more) pre-defined spatial niches, which require less active spatial competition, and hence yield the most robust coexistence. However, populations typically become spatially mixed, and can then still coexist by active spatial segregation and exclusion (**a**, **b**). Spatial patterns and fold changes are reported after 4 days in habitats of 20 mm linear extension. Simulation was performed using the MKS model with parameters as described in the Methods. **g**, **h**, Inoculation of mixed co-culture (LAB1 and LAB5, initial ratio: 1) in the centre (**g**) and around the edge (**h**) of a patch of circular geometry. **i**, **j**, Inoculation of mixed co-culture (LAB1 and LAB5, initial ratio: 1) in the centre (**i**) and edge (**j**) of a patch with spherical geometry. Both circular and spherical geometries also show coexistence. Note that other parameters such as nutrient concentration and initial cell density shift the selection curves (Fig. 4). Spatial patterns and fold changes are reported after 4 days in habitats of 20 mm radius. Simulation was performed using the MKS model with parameters as described in the Methods. Scale bars, 10 mm. **k**–**m**, Competition experiments with fast movers (blue, LAB2) and fast growers (red, LAB3), inoculated as either a mixed co-culture or unmixed at separate spots (close together or farther apart), at three initial ratios (fast grower/fast mover) = 10^{-2}, 1 and 10^{2}. The measured spatial patterns and selection functions are shown. When inoculated separately, the fast movers still encircle the fast growers and reach a higher abundance and density. The selection function crosses the unity fold change line, indicating coexistence. Consistent with the simulations in **c**–**f**, the fold change of the fast movers is higher at large R_0 when inoculated more distantly. These findings may be explained as follows: for separated inoculation, the fast movers have a (more) pre-defined spatial niche (location), which further limits their competition with the fast growers, allows them to reach a higher abundance, and hence increases their competitive advantage. Such a rationale is consistent with classical niche theory, which indicates that spatial niches limit between-organism competition. Taken together, both mixed and separated cultures can coexist in these spatial habitats. Scale bars, 10 mm.

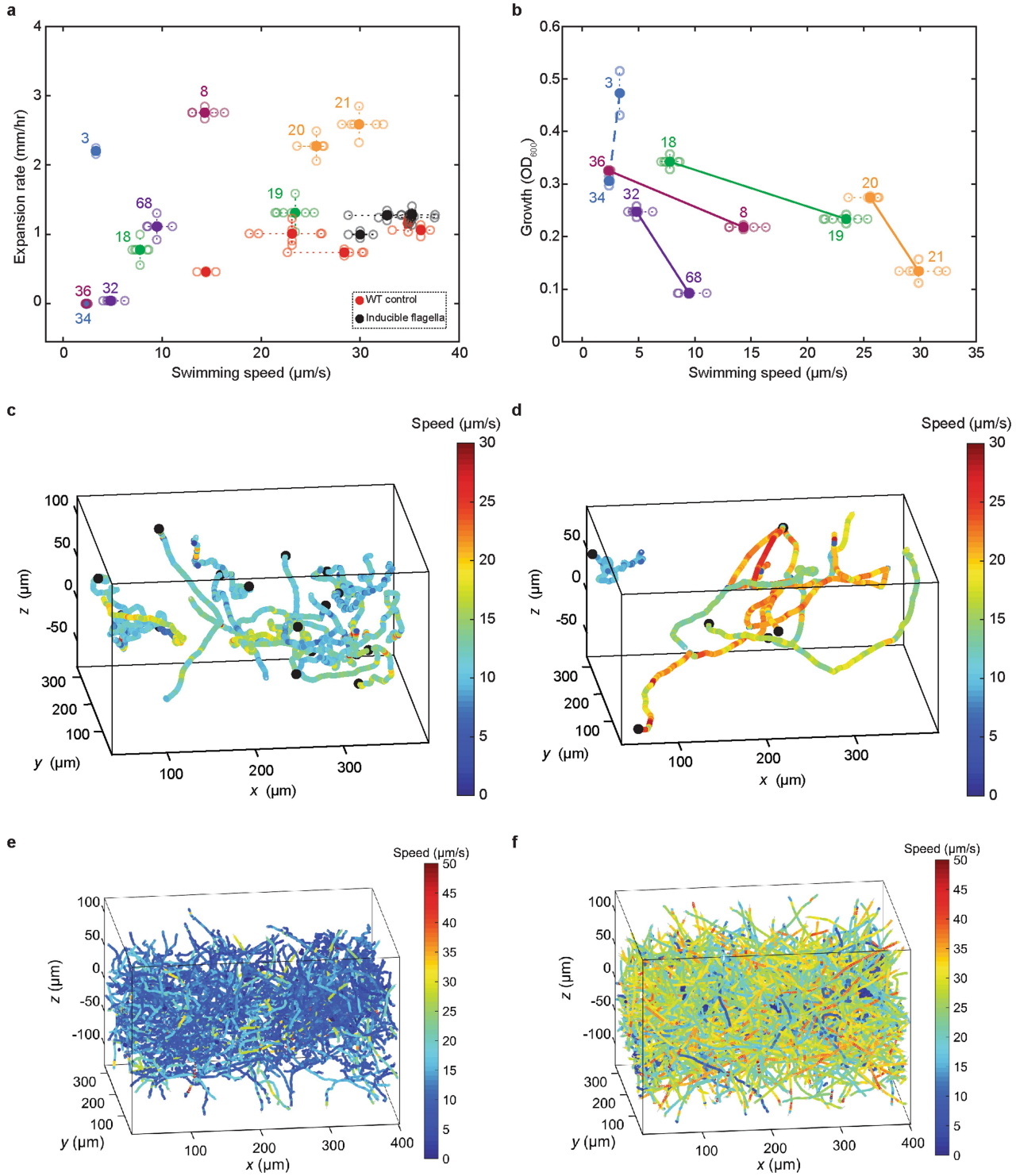

Extended Data Fig. 8 | See next page for caption.

Extended Data Fig. 8 | Average swimming speed of cells correlates with collective migration rate. a, Relation between average swimming speed of wild isolates in liquid rich medium (1%(w/v) TB) with their expansion rate in soft-agar motility assay (0.26% (w/v) agar). The trajectory and speed of each bacterial cell were extracted using a high-throughput three-dimensional cell-tracking method, from videos recorded at 15 Hz sampling rate[35]. Average swimming speeds were calculated from the full populations (that is, swimming and non-swimming). The cells were grown to their exponential phase in overnight TB culture and diluted into fresh TB medium. Open circles indicate expansion rates and mean swimming speeds (across all recorded trajectories) obtained from a single acquisition of an individual experiment. Filled circles indicate weighted-mean swimming speed across all repeated experiments (with the error-estimate weights) and mean expansion rate across two repeats (see 'Statistics and reproducibility' in the Methods). Cohabitant pairs bear the identical colour code. Red and black data points (open and filled circles) show the mean swimming speeds and expansion rates of flagella induction strain and its wild-type control (Extended Data Fig. 9). **b**, Trade-off between growth propensity (OD_{600} after 7.5 h, data shown in Fig. 2b and Extended Data Fig. 1f) and mean swimming speed in ECOR pairs. The observed growth–speed trade-off follows the pattern of the growth–migration trade-off shown in Figs. 2b, 4 out of 5 pairs show a difference in swimming speed and growth. Open and filled circles are defined as indicated in **a**. **c**, **d**, A subset of three-dimensional tracks of natural isolates A (ECOR18) (**c**) and B (ECOR19) (**d**) with a minimum duration of 20 s and a median speed larger than 10 μm s^{-1} are illustrated. The tracks were sampled from the full population shown in **e** and **f**. The starting point of each individual trajectory was marked by a black dot. Speed colour map shows the instantaneous speed at each point in space. **e**, **f**, Three-dimensional tracks of the total population of natural isolates A (**e**) and B (**f**). A total of 891 (A) and 1,019 (B) cell trajectories were tracked and recorded.

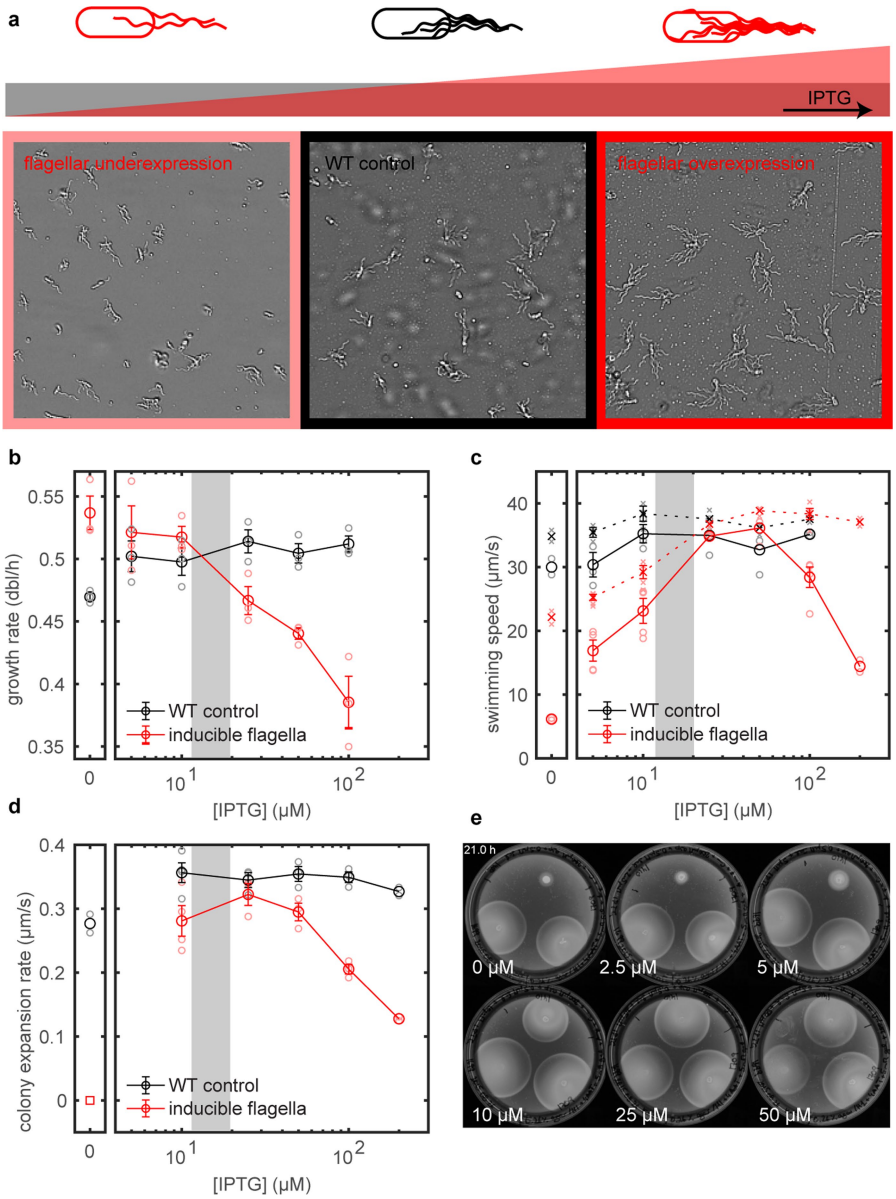

Extended Data Fig. 9 | Cost of motility and the growth–motility trade-off. We first estimated the synthesis and operating costs of the flagella that power motility. A single cell produces about 62,000 flagellin units (assuming 3.4 flagella per cell, each 7.3 μm long with helical pitch and radius of 2.5 μm and 0.25 μm[57], respectively, composed of 11 protofilaments with flagellin repeat distances of 5.2 nm[58]). For flagellin synthesis, we estimate the cost as 7.7×10^8 P per cell cycle (using 25 phosphate cleavages (P) per amino acid[59], 498 amino acids per flagellin). Using 47.7 kJ mol^{-1} for one phosphate cleavage[60], the minimum power for flagella synthesis then ranges from 1×10^{-14} W (slow growth, doubling time 100 min) to 4.3×10^{-14} W (fast growth, doubling time 24 min). The operating power of one flagellar motor is estimated at 1.5×10^5 pN nm s^{-1} = 1.5×10^{-16} W[61], resulting in 5.1×10^{-16} W for the whole cell. Thus, the cost of flagella expression is dominant. To estimate the corresponding growth penalty, we compute a cellular flagellin mass of 51 kg mol^{-1} × 62,000/R = 5.3 fg, given a flagellin molecular weight of 51 kDa and Avogadro's number, $R = 6 \times 10^{23}$. Assuming a total cellular protein mass of 100 fg (slow growth, doubling time 100 min) to 450 fg (fast growth, 24 min)[62], flagellin constitutes approximately 1.2% to 5.3% of the total protein mass of the cell. Assuming that growth costs are determined by protein synthesis, these numbers indicate that the growth penalty is significant, and provide a mechanistic rationale for a growth–motility trade-off. Other costs such as reduced membrane integrity and operating costs further increase this penalty. We investigated this issue experimentally, using new laboratory strains to allow expression control of flagella. **a**, Leifson stains showing flagellation for a wild-type control strain (TSS1709, 50 μM IPTG, black, middle) and a flagella induction strain (TSS1410; left, 10 μM IPTG, right, 100 μM IPTG). TSS1709 is a vector control, while TSS1410 carries an IPTG-inducible plasmid expressing the flagella master regulator FlhDC (pSJAB50) in an *flhDC* deletion background. In both strains, all chemoreceptors (*tar*, *tsr*, *tap*, *trp* and *aer*) and chemotaxis signalling genes (*cheAWRBYZ*) have been deleted and replaced by a plasmid expressing *cheAW*, *tar*, *tsr*, *cheRBYZ* (pTA6) to decouple them from *flhDC* control. **b**, Growth-rate dependence on IPTG induction for both strains. **c**, Average swimming speed of the full population (circles with solid lines) and of the motile population (crosses with dotted lines) as a function of IPTG induction. **d**, Colony expansion rate in soft-agar plates as a function of IPTG induction. The red square reflects the lack of expansion in the flagella induction strain in the first 24 h at 0 μM IPTG. We observed asymmetric expansion at later time points, which we attribute to mutations. In **b**-**d**, lines connect data points to guide the eye, and the grey area indicates the IPTG range in which the flagella induction strain mimics the wild-type properties. Small symbols show raw data, large symbols show averages of raw data, and error bars indicating the standard error of the mean are shown whenever $n > 2$. **e**, Soft-agar plates for various IPTG concentrations 21 h after inoculation with the wild-type control strain (bottom-right colony), the flagella induction strain (top colony) and a flagella overexpression strain that contains the inducible *flhDC* plasmid in addition to wild-type chromosomal *flhDC* (TSS1699, left colony).

Extended Data Table 1 | Motility genes of the cohabitant pair ECOR18–ECOR19 display various amino acid substitutions

gene	gene length	# of DNA substi - tutions	DNA substitutions	# of AA substi - tutions	AA substitutions
aer	1521	1	T546G	1	F182V
cheR	861	1	G608A	0	
dgcE	3318	116	G200A, C215T, A218G, T269C, C274T, A320G, G323A, A350C, G404A, G440A, T482G, A500T, G521A, A536G, G728T, A740G, A744C, T755G, A785G, T788C, C851G, T914A, T917C, C920G, A1022G, C1028T, G1079C, C1136T, A1184T, G1268C, C1271T, G1295T, C1338T, A1340G, C1457T, C1475T, A1481G, T1496G, A1505G, A1521G, C1523T, C1532T, T1538C, T1559C, C1622T, A1625G, G1628T, C1653A, A1655G, G1682T, C1694T, A1784G, T1883C, C1907T, C1922T, A1976T, C1979T, C2003T, T2075C, G2093A, A2129G, C2198T, C2201G, T2204G, C2261T, A2276G, T2282C, C2285T, T2312C, T2315C, C2321T, T2327C, G2330T, C2348T, C2357T, C2360T, C2381A, A2390C, T2393G, G2413A, T2414C, T2432C, T2456A, A2523G, A2544G, A2619C, G2642A, A2750G, A2771C, T2786A, C2804A, T2825C, G2843C, A2885T, A2888G, A2889C, A2948T, C2951A, A2974G, C3008A, A3011G, T3012C, A3016G, T3017C, A3059G, A3077G, A3113T, C3143T, G3164A, G3176A, A3194C, C3204T, G3206A, C3251T, T3254G, C3296T	16	T91I, M248L, T507A, Q551K, S804N, I841V, T848A, I873L, D928E, E961D, I963L, D983E, N991S, F1004L, N1005S, D1084E
dgcN	1227	1	A272T	0	
dgcQ	1695	39	G134A, A297G, C302T, C342A, T383C, G386A, G410A, A491G, A584T, G624A, G635A, G738A, A740T, A863T, A972G, G1023A, C1038T, C1143T, C1151T, T1167C, T1259G, T1263A, C1307T, T1319C, A1403T, T1412C, C1466T, C1473G, G1484A, T1487C, C1509T, C1532T, C1535T, C1566T, C1577T, C1592T, A1637G, C1658T, C1664T	10	N99D, Q114K, V208I, E246N, L287F, N324D, V341M, R381W, L421M, Q491E
dgcT	1359	1	A972G	1	I324V
dgcZ	891	2	C299A, G541T	2	D99E, G180V
flgE	1209	1	C1169T	0	
flgF	756	1	G522A	1	D174N
flgH	699	2	A74G, T386G	1	I24M
flgK	1644	1	G1027A	1	G342D
flhA	2079	1	G1997A	0	
fliA	720	5	A47G, G526A, T536C, C632T, G635A	1	S175N
fliE	315	6	G68A, T74A, G83A, G102A, T134A, T152C	2	D24E, A34T
fliF	1659	13	A275G, A293G, G575A, C593G, A614G, C638T, T686C, T722G, A743G, T755A, G797A, A1204C, C1431A	2	K401T, R477S
fliG	996	2	A785G, A803G	0	
fliH	687	11	T176G, A204G, A332G, G380A, C476T, G482A, A485G, A488G, C500G, A536T, A578C	1	K68E
fliJ	444	1	C161T	0	
fliK	1128	41	A20G, T38C, A40C, G42A, T125A, C204G, G207T, C253T, G254T, A290G, A305G, C335A, G342A, A345C, T365C, G368T, C389T, T448C, G449A, A515T, T533C, G545A, A608G, A614G, C628A, G689T, G794A, C818T, A845G, A848G, G858A, T875C, G887C, G890C, T902G, T995G, T1024C, T1066C, A1080T, C1091T, C1100T	14	N13T, A14T, L68V, A69S, P84L, N111K, A114T, K115Q, V149A, A209D, V286I, V341A, L355P, I360L
fliL	465	6	C16T, A152G, C170T, C185T, G206A, G215A	1	T5I
fliM	1005	17	C314A, T317C, G320T, T353C, A356G, T362C, G509A, T563C, C566T, T659A, G779A, C785G, T842C, C869T, C896T, G902A, T923C	0	
fliN	414	13	T65G, A74G, C89T, A90G, C92A, T131C, T134A, G251A, C254A, A287G, T380C, T386C, A392G	1	S30G
fliO	366	7	C11T, C48T, T104C, T123C, T133C, T329C, A337G	3	P16S, V44A, N112S
fliP	738	18	A23C, G42A, A128G, C203T, T231C, A239G, A272G, G278A, G308A, T317C, C362A, C428T, T491C, T572C, T599A, G620A, A641C, A647C	1	V14I
fliS	411	6	G71A, A125G, G173A, A203G, C284T, G374T	0	
fliT	366	5	C6G, A77G, G110A, C172T, T320C	2	H2D, T57I
motB	927	1	A164G	0	
tap	1602	1	T1073C	0	
tar	1662	1	C1274T	0	
tsr	1665	28	A425G, C467T, G515A, G519A, T531C, C836A, T971C, T983C, C1016T, C1049T, T1070C, C1163T, C1196T, T1202A, T1220C, C1226T, T1232C, A1283G, A1313C, C1343T, T1376A, T1430C, T1487C, G1568T, A1597C, A1611G, A1628C, G1631A	6	D173N, Y177H, S278R, Q522H, N532T, T537A

Genomic sequences of ECOR18(A) and ECOR19(B) were compared as described in the Methods. In total, 6,923 DNA substitutions within genes and 1,054 DNA substitutions in intergenic regions were detected among the cohabitant pair. Motility genes (as defined below) exhibited 349 DNA substitutions and 67 amino acid substitutions, that is, 30 out of 63 motility genes had at least 1 DNA substitution and 19 out of 63 at least 1 amino acid substitution. Motility genes: *aer*, *bdm*, *cdgI*, *chaC*, *cheA*, *cheB*, *cheR*, *cheW*, *cheY*, *cheZ*, *csrA*, *dgcE*, *dgcJ*, *dgcN*, *dgcQ*, *dgcT*, *dgcZ*, *dosC*, *flgA*, *flgB*, *flgC*, *flgD*, *flgE*, *flgF*, *flgG*, *flgH*, *flgI*, *flgJ*, *flgK*, *flgL*, *flgM*, *flgN*, *flhA*, *flhC*, *flhD*, *fliA*, *fliC*, *fliD*, *fliE*, *fliF*, *fliG*, *fliH*, *fliJ*, *fliK*, *fliL*, *fliM*, *fliN*, *fliO*, *fliP*, *fliS*, *fliT*, *malE*, *motA*, *motB*, *mqsR*, *pdeH*, *tap*, *tar*, *trg*, *tsr*, *ycgR*, *yehP* and *yfiR* (https://biocyc.org/ECOLI/NEW-IMAGE?object=BC-5.3; obtained, 27 February 2019). A number of interesting mutations are observed within these data. For instance, amino acid changes are found in the chemotaxis gene *fliA*, which is known to regulate the expression of flagella genes. In addition, we found mutations in chemotaxis sensory genes (for example, *tsr* and *aer*) and flagella genes (for example, *fliE* and *fliF*). We also observed a substantial number of mutations in the dgc genes, which are involved in regulation of flagella gene expression upon the switch between the motile and sessile phases of the *E. coli* life cycle, through the modulation of the intracellular cyclic di-GMP concentration.

nature research

Corresponding author(s): *Double-blind peer review submissions: write DBPR and your manuscript number here instead of author names.*

Reporting Summary

Nature Research wishes to improve the reproducibility of the work that we publish. This form provides structure for consistency and transparency in reporting. For further information on Nature Research policies, see Authors & Referees and the Editorial Policy Checklist.

Statistical parameters

When statistical analyses are reported, confirm that the following items are present in the relevant location (e.g. figure legend, table legend, main text, or Methods section).

n/a	Confirmed	
☐	☒	The exact sample size (*n*) for each experimental group/condition, given as a discrete number and unit of measurement
☐	☒	An indication of whether measurements were taken from distinct samples or whether the same sample was measured repeatedly
☒	☐	The statistical test(s) used AND whether they are one- or two-sided *Only common tests should be described solely by name; describe more complex techniques in the Methods section.*
☒	☐	A description of all covariates tested
☒	☐	A description of any assumptions or corrections, such as tests of normality and adjustment for multiple comparisons
☒	☐	A full description of the statistics including central tendency (e.g. means) or other basic estimates (e.g. regression coefficient) AND variation (e.g. standard deviation) or associated estimates of uncertainty (e.g. confidence intervals)
☒	☐	For null hypothesis testing, the test statistic (e.g. *F*, *t*, *r*) with confidence intervals, effect sizes, degrees of freedom and *P* value noted *Give P values as exact values whenever suitable.*
☒	☐	For Bayesian analysis, information on the choice of priors and Markov chain Monte Carlo settings
☒	☐	For hierarchical and complex designs, identification of the appropriate level for tests and full reporting of outcomes
☒	☐	Estimates of effect sizes (e.g. Cohen's *d*, Pearson's *r*), indicating how they were calculated
☐	☒	Clearly defined error bars *State explicitly what error bars represent (e.g. SD, SE, CI)*

Our web collection on statistics for biologists may be useful.

Software and code

Policy information about availability of computer code

Data collection	The tile images of bacterial gel samples were acquired using custom-made scripts of the automated imaging software μManager (version 1.4).
Data analysis	The tile images of bacterial gel samples were combined on Java platform (versions SE7 and SE8) and the data analyses on these images were conducted using custom-made Java scripts and ImageJ (version 1.4 and 1.5). All analyses of fold-change in population ratio data were carried out using custom-made codes on MATLAB (R2013b,R2016b) platform. Colony counting data were acquired by manual counting in ImageJ. 3D tracking traces were analyzed with custom-made codes on MATLAB (R2013a,R2017a,R2018b). Genomic analyses of ECOR18 and ECOR19 were performed using SRA Toolkit version 2.9.2, sickle version 1.33, botwie2 version 2.3.4.3, Picard version 2.18.25, GATK version 4.1.0.0, snpsift version 4.3t, VCFtools version 0.1.15, SnpEff version 4.3t, and custom scripts written in Python version 3.6.7 and BioPython version 1.72.

For manuscripts utilizing custom algorithms or software that are central to the research but not yet described in published literature, software must be made available to editors/reviewers upon request. We strongly encourage code deposition in a community repository (e.g. GitHub). See the Nature Research guidelines for submitting code & software for further information.

Data

Policy information about availability of data

All manuscripts must include a data availability statement. This statement should provide the following information, where applicable:

- Accession codes, unique identifiers, or web links for publicly available datasets
- A list of figures that have associated raw data
- A description of any restrictions on data availability

The data that support the findings of this study are available from the corresponding author upon reasonable request.

Field-specific reporting

Please select the best fit for your research. If you are not sure, read the appropriate sections before making your selection.

☒ Life sciences ☐ Behavioural & social sciences ☐ Ecological, evolutionary & environmental sciences

For a reference copy of the document with all sections, see nature.com/authors/policies/ReportingSummary-flat.pdf

Life sciences study design

All studies must disclose on these points even when the disclosure is negative.

Sample size	Experiment to experiment variability for most measured quantities (growth and migration rates, swimming speed, population fold change) were found to be small (<20% across 2-6 samples). Thus we replicated most experiments at least once from two or more independent overnight cultures so that the total number of replicates n over m overnight cultures were greater than two (n>m>2). All replicates produced similar results. Imaging of flagellar staining (bright field) and migration rings (dark field) was conducted once. Exact sample size for all experiments are given in the section "Statistics and Reproducibility" in Methods.
Data exclusions	No data were excluded from analyses.
Replication	All experimental findings were successfully reproduced by employing two or more replicates of each bacterial sample.
Randomization	We did not randomize strain groups. Randomization was not applicable as strains were allocated according to different conditions such as culturing conditions.
Blinding	We did not use blinding when performing the experiments and in the data analysis, as the data acquisition and analysis were done in different conditions.

Reporting for specific materials, systems and methods

Materials & experimental systems

n/a	Involved in the study
☒	☐ Unique biological materials
☒	☐ Antibodies
☒	☐ Eukaryotic cell lines
☒	☐ Palaeontology
☒	☐ Animals and other organisms
☒	☐ Human research participants

Methods

n/a	Involved in the study
☒	☐ ChIP-seq
☒	☐ Flow cytometry
☒	☐ MRI-based neuroimaging